# Determination of the macroscopic optical properties of snow based on exact morphology and direct pore-level heat transfer modeling

Sophia Haussener,[1] Mathias Gergely,[2,3] Martin Schneebeli,[2] and Aldo Steinfeld[4,5]

Received 4 January 2012; revised 30 May 2012; accepted 5 June 2012; published 27 July 2012.

[1] A multiscale methodology for the determination of the macroscopic optical properties of snow is presented. It consists of solving the coupled volume-averaged radiative transfer equations for two semi-transparent phases – ice and air – by Monte Carlo ray tracing in an infinite slab via direct pore-level simulations on the exact 3D microstructure obtained by computed tomography. The overall reflectance and transmittance are computed for slabs of five characteristic snow types subjected to collimated and diffuse incident radiative flux for wavelengths 0.3–3 $\mu$m. The effect of simplifying the snow microstructure and/or the radiative transfer model is elucidated by comparing our results to (*i*) a homogenized radiation model and considering a particulate medium made of optical equivalent grain size spheres (DISORT), or (*ii*) a multiphase radiation model considering a packed bed of identical overlapping semi-transparent spheres. The calculations are experimentally validated by transmittance measurements. Significant differences in the macroscopic optical properties are observed when simplifying the snow morphology and the heat transfer model (i.e., homogenized versus multiphase). The proposed approach allows – in addition to determine macroscopic optical properties based on the exact morphology and obtained by advanced heat transfer model – for detailed understanding of radiative heat transfer in snow layers at the pore-scale level.

**Citation:** Haussener, S., M. Gergely, M. Schneebeli, and A. Steinfeld (2012), Determination of the macroscopic optical properties of snow based on exact morphology and direct pore-level heat transfer modeling, *J. Geophys. Res.*, *117*, F03009, doi:10.1029/2012JF002332.

## 1. Introduction

[2] Radiative characterization of snowpack is of importance to determine the overall energy/water balance between ground and atmosphere in snow covered regions [*Wiscombe and Warren*, 1980; *Marks and Dozier*, 1992; *Marks et al.*, 1998; *Aoki et al.*, 2000; *Flanner and Zender*, 2006; *Warren et al.*, 2006; *Kuipers Munneke et al.*, 2009; *Gardner and Sharp*, 2010], for climate models investigating surface-atmosphere energy balances [*Douville et al.*, 1995; *Roesch et al.*, 2002; *Jacobson*, 2004], and for remote sensing applications to map snow cover and to estimate snow water equivalents [*Foster and Rango*, 1989; *Nolin and Dozier*, 2000].

[3] One of the key elements in these applications has been to adequately account for the microstructure of snow in the determination of its optical properties, as snow accumulated on the ground generally consists of a complex 3D microstructure of ice and air [*Good*, 1987; *Dominé et al.*, 2003; *Flin et al.*, 2004; *Schneebeli and Sokratov*, 2004; *Fierz et al.*, 2009]. A common approach is to consider an optical equivalent grain size (OED) derived from the specific surface area (SSA, the air-ice phase boundary per total snow volume) of the actual 3D snow microstructure [*Wiscombe and Warren*, 1980; *Matzl and Schneebeli*, 2006; *Painter et al.*, 2007; *Gallet et al.*, 2009]. However, the accurate determination of OED is challenging and its estimations from visual micrograph examination lead to significantly smaller grain sizes than those estimated by traditional methods (e.g., mean major axis length of the broken snow structure estimated by hand-lens measurements) [*Aoki et al.*, 2000]. Additionally, grain sizes do not correlate with OED for complex snow structures such as rounded snow, facets, and polycrystals [*Painter et al.*, 2007]. Moreover, calculated reflectance for non-spherical, specific grain shaped ice particles of snow (e.g., cubes, cylinders, or hexagonal plates) can differ substantially from that obtained for the respective OED spheres at visible and near infrared (NIR) wavelengths [*Xie et al.*, 2006; *Picard et al.*, 2009]. In contrast, *Gallet et al.* [2009] found minor effects of grain sizes on reflectance measurements in natural snow and *Grenfell and Warren* [1999] reported successful determination of direction-independent radiative properties

[1]Institute of Mechanical Engineering, EPFL, Lausanne, Switzerland.
[2]WSL Institute for Snow and Avalanche Research SLF, Davos, Switzerland.
[3]Institute of Environmental Physics, Heidelberg University, Germany.
[4]Department of Mechanical and Process Engineering, ETH Zurich, Zurich, Switzerland.
[5]Solar Technology Laboratory, Paul Scherrer Institute, Villigen, Switzerland.

Corresponding author: S. Haussener, Institute of Mechanical Engineering, EPFL, 1015 Lausanne, Switzerland. (sophia.haussener@epfl.ch)


0148-0227/12/2012JF002332

of a random collection of infinitely long cylinders by using OED spheres and same density as the snow sample measured. These partially contradicting findings indicate the need for in-depth pore-level analysis of the interaction of radiation with snow and for quantifying the error introduced in snow's radiative properties by morphological simplifications, which evidently vary with different snow types.

[4] The widely used DISORT model [*Stamnes et al.*, 1988] for radiative heat transfer in porous media solves a homogenized radiative transfer equation (RTE) with apparent radiative properties, which account for the snow microstructure by assuming a collection of independently scattering dilute (OED) spheres with the same volume fraction as the original snow sample. Thus, by applying a homogenized approach, DISORT, simplifies the snow morphology and neglects the two-phase nature of snow. DISORT has been applied to various investigations related to snow physics [e.g., *Fily et al.*, 1997; *Jin and Simpson*, 1999; *Glendinning and Morris*, 1999; *Nolin and Dozier*, 2000; *Xie et al.*, 2006; *Painter and Dozer*, 2004; *Gallet et al.*, 2009]. However, the error introduced by the morphological and radiative transfer simplifications, which evidently vary with the type of snow, has remained for the most part unknown. DISORT results have not yet been compared to pore-level radiative transfer simulations where the exact 3D snow microstructure and the multiphase nature of snow have been accounted for explicitly. Hence, previous studies are of limited use for understanding the influence of snow morphology on its radiative properties.

[5] A first approach to account for the complex morphology of snow was introduced in tomography-based studies [*Kaempfer et al.*, 2007; *Bänniger et al.*, 2008], where computed tomography (CT) images of the snow microstructure were used as input for the reflectance and transmittance determination by a phenomenological ray-tracing approach. Recently, a more advanced phenomenological multiphase heat transfer model has been proposed for the radiative characterization of multiphase media in the limit of geometrical optics, assuming independent scattering and neglecting diffraction [*Lipiński et al.*, 2010a, 2010b]. The model is derived by applying volume-averaging theory to RTEs valid within each phase and applying the appropriate phase boundary conditions. The volume-averaged RTEs are based on the energy balance inside the 2-phase media, while the RTE valid for a single phase can be derived – under certain assumptions – directly from Maxwell's equations for discrete random media [*Mishchenko*, 2008; *Mishchenko et al.*, 2011]. The volume averaged RTEs have, so far, not been tested against Maxwell's equations. The volume averaged RTEs have been used to determine the radiative characteristics of reticulate porous ceramics [*Petrasch et al.*, 2007; *Haussener et al.*, 2010a; *Haussener and Steinfeld*, 2012] and packed beds [*Haussener et al.*, 2009, 2010b] by direct pore-level simulations (DPLS, also called direct numerical simulations) on the CT scans and, partially, validated by estimation of the radiative properties by spectroscopic measurements. The novel phenomenological multiphase heat transfer model allows investigating the macroscopic, surface radiative properties and, in addition to previous common snow radiation models, investigating detailed discrete-scale radiative properties and heat transfer at the pore-level scale of complex snowpacks in the limit of geometrical optics, assuming independent scattering and neglecting diffraction.

[6] Here, we apply a multiscale approach to snow (pure, without soot or other impurities), consisting of: (*i*) CT of snow samples to obtain the 3D geometrical representation of their porous microstructure ; (*ii*) use of the CT-determined digital 3D geometry (microstructure) in DPLS for solving the RTEs by collision-based Monte Carlo ray-tracing at the pore scale; (*iii*) extraction of the effective (volumetric) radiative properties of the porous medium, namely: the extinction coefficients, the scattering coefficients, and the scattering phase functions; (*iv*) incorporation of the effective radiative properties in the solution of the volume-averaged RTEs at the continuum scale to determine (surface) radiative properties such as overall reflectance and transmittance of an infinite snow slab. This CT-based Monte Carlo methodology is referred to as the "CTMC" model. Its results can be considered as approaching the exact solution within the limits of the numerical truncation error, the accuracy of geometrical representation (i.e., statistical variations and CT resolution), and the simplifications in the radiation model (geometric optics, independent scattering, neglecting diffraction). The reflectance and transmittance obtained by CTMC simulations are compared to those obtained by DISORT, which solves a homogenized RTE and simplifies the snow structure by OED independent spheres, and to those obtained by a multiphase Monte Carlo approach also applied to the simplified OED snow structure. This allows quantitatively investigating the influence of snow morphology and radiation model (homogenized versus multiphase approach) on the radiative properties. Calculations are carried out for 4 cm-thick infinite (in the other two dimensions) snow slabs of five characteristic snow types. As an example, in-depth analysis of volumetric radiative heat transfer at the pore-level scale (discrete-scale) is given to highlight the possibility of using CTMC to investigate a completely new set of research problems. Transmittance calculations are compared with measured values for seven additional snow types at NIR wavelengths to evaluate the different modeling approaches.

## 2. Radiative Transfer Within Snow

[7] Radiation interaction within a participating medium is generally described by the radiative transfer equation (RTE) [*Modest*, 2003],

$$\hat{\mathbf{s}}\cdot\nabla L(\mathbf{x},\hat{\mathbf{s}}) = -\beta_{\mathrm{int}}L(\mathbf{x},\hat{\mathbf{s}}) + n^2\kappa L_{\mathrm{b}}(\mathbf{x},\hat{\mathbf{s}}) + \frac{\sigma_{\mathrm{s}}}{4\pi}\int_{4\pi} L(\mathbf{x},\hat{\mathbf{s}}_{\mathrm{in}})\Phi(\hat{\mathbf{s}}_{\mathrm{in}},\hat{\mathbf{s}})\mathrm{d}\Omega_{\mathrm{in}}, \tag{1}$$

where the intensity, $L$, is attenuated due to extinction (first term on right hand side) and is augmented due to internal emission and incoming scattering (second and third terms on right hand side). Internal emission can be neglected for the temperatures and wavelength region considered. Equation (1) is valid in each phase of a two-phase medium, such as snow composed of two semi-transparent phases: air and ice. RTE has been derived from Maxwell's equations and can, therefore, be assumed to be microphysical in the limit of assumed simplifications [*Mishchenko*, 2008; *Mishchenko et al.*, 2011]. Volume averaging of a RTE for each phase

(air and ice) in the limit of geometrical optics leads to two coupled volume-averaged RTEs as described in *Lipiński et al.* [2010a, 2010b] and given by,

$$\begin{aligned}\hat{\mathbf{s}}\cdot\nabla I_i(\mathbf{x},\hat{\mathbf{s}}) = &-\beta_i I_i(\mathbf{x},\hat{\mathbf{s}}) + n_i^2\kappa_i I_{\mathrm{b},i}(\mathbf{x},\hat{\mathbf{s}}) \\ &+\frac{\sigma_{\mathrm{s},ii}}{4\pi}\int_{4\pi} I_i(\mathbf{x},\hat{\mathbf{s}}_{\mathrm{in}})\Phi_{ii}(\hat{\mathbf{s}}_{\mathrm{in}},\hat{\mathbf{s}})\mathrm{d}\Omega_{\mathrm{in}} \\ &+\frac{\sigma_{\mathrm{s},ji}}{4\pi}\int_{4\pi} I_j(\mathbf{x},\hat{\mathbf{s}}_{\mathrm{in}})\Phi_{ji}(\hat{\mathbf{s}}_{\mathrm{in}},\hat{\mathbf{s}})\mathrm{d}\Omega_{\mathrm{in}} \qquad i,j=1,2;\mathrm{i}\neq\mathrm{j},\end{aligned} \tag{2}$$

where $I_i$ is the volume averaged intensity, $I_i = \frac{1}{V}\int_V L_i \mathrm{d}V$, and

$$\sigma_{\mathrm{s},ii} = \sigma_{\mathrm{s,refl},i} + \sigma_{\mathrm{s},i}, \tag{3}$$

$$\Phi_{ii} = \sigma_{\mathrm{s},ii}^{-1}\left(\Phi_{\mathrm{refl},i}\sigma_{\mathrm{s,refl},i} + \Phi_i\sigma_{\mathrm{s},i}\right), \tag{4}$$

$$\beta_i = \kappa_i + \sigma_{\mathrm{s},ii} + \sigma_{\mathrm{s},ij} = \beta_{\mathrm{int},i} + \sigma_{\mathrm{s,refl},i} + \sigma_{\mathrm{s},ij}, \tag{5}$$

$$\beta_{\mathrm{int},i} = \kappa_i + \sigma_{\mathrm{s},i}. \tag{6}$$

$\beta_{\mathrm{int},i}$, $\kappa_i$, $\sigma_{\mathrm{s},i}$ and $\Phi_i$ are the internal extinction coefficient, internal absorption coefficient, internal scattering coefficient, and internal scattering phase function of the bulk material forming phase $i$, respectively. $\sigma_{\mathrm{s,refl},i}$ and $\Phi_{\mathrm{refl},i}$ are associated with internal reflections and internal scattering within phase $i$, respectively, and $\sigma_{\mathrm{s},ij}$ and $\Phi_{ij}$, $i \neq j$, are associated with internal refraction from phase $i$ to phase $j$. $\sigma_{\mathrm{s},i}$, $\kappa_i$, and $\Phi_i$ are determined by applying an appropriate theory, e.g., Mie [*Bohren and Huffman*, 2004]. It is important to note that the internal one-phase radiative properties ($\beta_{\mathrm{int},i}$, $\kappa_i$, $\sigma_{\mathrm{s},i}$ and $\Phi_i$) depend solely on the material properties of the phases involved while the two-phase radiative properites ($\sigma_{\mathrm{s,refl},i}$, $\sigma_{\mathrm{s},ij}$, $\Phi_{\mathrm{refl},i}$, and $\Phi_{ij}$) depend solely on the morphology of the multiphase media. The internal one-phase radiative properties might be zero for non-absorbing and non-scattering phases (such as air) but the two-phase radiative properties are still nonzero. The two-phase medium morphology-associated properties, $\sigma_{\mathrm{s,refl},i}$, $\sigma_{\mathrm{s},ij}$, $\Phi_{\mathrm{refl},i}$, and $\Phi_{ij}$ are derived from the corresponding probability distribution functions [*Tancrez and Taine*, 2004; *Haussener et al.*, 2009]. The coupled, volume-averaged RTEs are a phenomenological approach based on energy balances inside the two-phase media and has not been validated against the exact solution of Maxwell's equations. CTMT for the determination of the effective properties and their incorporation in the two coupled, volume-averaged RTEs is described in section 2.1.

[8] Alternatively, the multiphase 3D structure can be approximated as a homogenized continuum medium by incorporating apparent scattering/absorption coefficients and apparent scattering phase function [*Modest*, 2003],

$$\begin{aligned}\hat{\mathbf{s}}\cdot\nabla I(\mathbf{x},\hat{\mathbf{s}}) = &-\beta_{\mathrm{a}} I(\mathbf{x},\hat{\mathbf{s}}) + n^2\kappa_{\mathrm{a}} I_{\mathrm{b}}(\mathbf{x},\hat{\mathbf{s}}) \\ &+\frac{\sigma_{\mathrm{s,a}}}{4\pi}\int_{4\pi} I(\mathbf{x},\hat{\mathbf{s}}_{\mathrm{in}})\Phi_{\mathrm{a}}(\hat{\mathbf{s}}_{\mathrm{in}},\hat{\mathbf{s}})\mathrm{d}\Omega_{\mathrm{in}}.\end{aligned} \tag{7}$$

The asymmetry factor,

$$g = \frac{1}{4\pi}\int_{4\pi}\Phi_{\mathrm{a}}(\mu_{\mathrm{s}})\mu_{\mathrm{s}}\mathrm{d}\Omega, \tag{8}$$

with $\mu_{\mathrm{s}}$ denoting the cosine of the scattering angle, is used to characterize the directionality of the phase function. This approach is examined with DISORT in section 2.2 [*Stamnes et al.*, 1988]. DISORT also assumes independent scattering.

### 2.1. Computed Tomography Based Monte Carlo

[9] The multiscale radiation problem is solved in two steps. First, DPLS is carried out at the pore scale on the 3D snow microstructure obtained by CT to determine the effective radiative properties $\sigma_{\mathrm{s,refl},i}$, $\sigma_{\mathrm{s},ij}$, $\Phi_{\mathrm{refl},i}$, and $\Phi_{ij}$, These properties are then incorporated in the system of equation (2), which is solved at the continuum scale to determine the macroscopic optical properties. We give a short summary only, an extended description of the methodology can be found in *Tancrez and Taine* [2004] and *Haussener et al.* [2009].

[10] *Pore-scale domain.* Geometrical optics are assumed since the characteristic size parameter $\pi d/\lambda \gg 1$ [*Modest*, 2003]. This assumption needs to be carefully considered when interpreting the results since deviations between results obtained by geometric optics and Maxwell's equations might differ significantly at relatively large characteristic size parameters, although largely dependent on particle shape [*Mishchenko et al.*, 2011]. Diffraction is neglected as radiation is diffracted predominantly in forward scattering direction within a small solid angle. Additionally, independent scattering is assumed. This assumption is controversial and has to be considered when interpreting the results as comparison of independent scattering and dependent scattering models [*Mishchenko*, 1994; *Mishchenko and Macke*, 1997; *Haussener et al.*, 2009] might lead to noticeable differences at relatively large characteristic particle sizes as well as relatively large volume fractions or porosities. The collision-based Monte Carlo ray-tracing method is used [*Farmer and Howell*, 1998] in combination with radiative distribution functions for semitransparent media [*Tancrez and Taine*, 2004; *Haussener et al.*, 2009]. A large number of stochastic rays uniformly distributed within a representative elementary volume (REV) of the snow samples are isotropically emitted to simulate radiation incidence at the boundaries. Rays are attenuated at the fluid-solid phase boundary and undergo either reflection or refraction. Additionally, rays are internally (within each semitransparent phases) scattered or absorbed. The distance between emission (radiation incidence at boundary) and collision points (for absorption and/or scattering), and the angle of incidence at the interface are recorded for each ray and contribute to the corresponding probability density functions. These statistical functions are directly related to the effective radiative properties of the two-phase medium - $\beta_i$, $\sigma_{\mathrm{s,refl},i}$, $\sigma_{\mathrm{s},ij}$, $\Phi_{\mathrm{refl},i}$, and $\Phi_{ij}$ - and are input to the following continuum model calculations.

[11] *Continuum domain.* The 3D computational domain for the determination of the macroscopic optical properties, i.e., reflectance, transmittance and absorptance, is schematically depicted in Figure 1. It consists of an infinite slab of snow with thickness $l_{\mathrm{slab}}$ exposed to an incident radiative heat

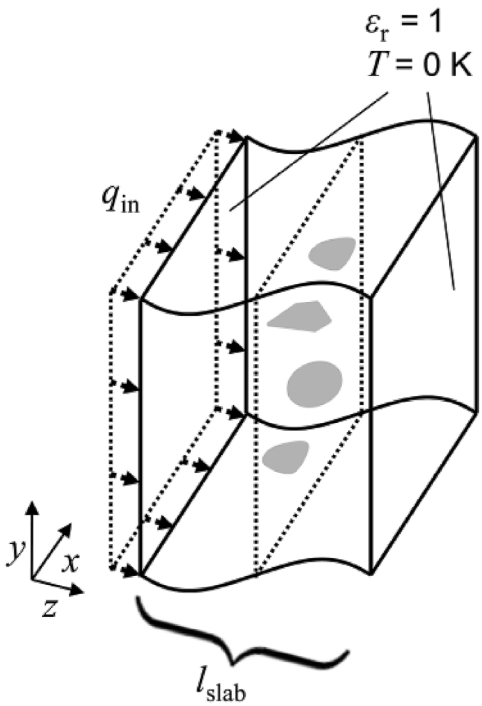


**Figure 1.** Schematic of the 3D continuum domain, consisting of an infinite snow slab of thickness $l_{slab}$ exposed to incident radiative heat flux $q_{in}$, which is either diffuse or collimated parallel to the $z$-axis. The lateral edges of the slab are assumed infinitely large, equal to a periodic boundary. The inlet and outlet faces are exposed to non-participating surroundings at $T = 0$ K and $\varepsilon_r = 1$.

flux $q_{in}$. Two cases are considered: (*i*) $q_{in}$ is diffuse, and (*ii*) $q_{in}$ is collimated parallel to the $z$-axis. The lateral edges of the slab are assumed infinitely large and equal to a periodic boundary. The inlet and outlet faces are exposed to non-participating surroundings at $T = 0$ K and $\varepsilon_r = 1$. Path length Monte Carlo is used to solve the two coupled volume-averaged RTEs, equation (2) [*Petrasch et al.*, 2011], using the previously determined effective radiative properties. Overall reflectance $R$, transmittance $Tr$, and absorptance $A$, are inlet ($z = 0$) and outlet ($z = l_{slab}$) area-averaged, and defined by:

$$R = \frac{\overline{q_1^-}(z=0) + \overline{q_2^-}(z=0)}{q_{in}}, \tag{9}$$

$$Tr = \frac{\overline{q_1^+}(z=l_{slab}) + \overline{q_2^+}(z=l_{slab})}{q_{in}}, \tag{10}$$

$$A = 1 - R - Tr, \tag{11}$$

where $\overline{q_i^j}$ denotes the radiative flux averaged over the cross-sectional area in forward or backward direction ($j$: +, -), and in the void or solid phase ($i$: 1, 2). Thus, $R$ and $Tr$ are the fractions of incident radiative flux leaving the slab at $z = 0$ and $z = l_{slab}$ respectively.

### 2.2. DISORT Model

[12] The RTE for a plane-parallel layered continuum medium, equation (7), is solved by using DISORT based on the discrete ordinate method [*Stamnes et al.*, 1988]. Internal emission is neglected in the visible and NIR spectrum. The snow structure is approximated by a random collection of spheres with the same specific surface area (SSA) and porosity as that of the real 3D snow structure, e.g., similar to *Grenfell and Warren* [1999]. Note that this snow structure approximation features a different grain number density than the real 3D snow structure. The apparent radiative properties, namely $\beta_a$, $\sigma_{s,a}$, and $\Phi_a$, are the pore-scale input parameters and calculated by Mie theory [*Bohren and Huffman*, 2004]. Apparent scattering albedo ($=\sigma_{s,a}/\beta_a$) and scattering phase function only depend on the optically equivalent snow grain size $d_{ice} = 6(1-\varepsilon)/A_0$, with $A_0$ being the specific surface area of snow per total snow volume, and the refractive indexes of air and ice. The computational domain depicted in Figure 1 is used for the continuum calculations, where snow density (porosity) and layer thickness are incorporated in the optical layer depth ($=\int_0^z \beta_a dz'$). The source integral in equation (7) is approximated by a quadrature sum over the polar directions. The computational accuracy increases with the number of polar angles.

[13] Both CTMC (section 2.1) and DISORT (section 2.2) involve determining scattering and absorption properties at the pore scale and use them in subsequent calculations for the determination of macroscopic optical properties at the continuum scale. However, there is a fundamental difference between the two approaches. CTMC accounts for the complex microstructure and describes the scattering behavior for each phase by two sets of phase functions and scattering coefficients, each accounting for (total) reflection and refraction. In contrast, DISORT assumes a homogenous collection of spheres and considers an overall apparent scattering phase function and apparent scattering and extinction coefficients.

## 3. Results for Five Characteristic Snow Types

[14] First, CT-based morphological characterization of five characteristic snow samples are obtained to be used as input for the models: (*i*) digitalized CT data as direct input for the CTMC model and (*ii*) calculated morphological characteristics, such as porosity and SSA (given in Table 2), as input for DISORT. Second, the intrinsic radiative properties of the two phases involved (ice and air) are briefly reviewed. Third, the effective (pore-level) radiative properties for the two approaches are calculated. Fourth, the macroscopic optical properties, reflectance and transmittance, are calculated based on the two models and compared. The pore-scale absorption data, allowing for in-depth analysis of volumetric radiative heat transfer at the pore-level and exclusively obtained by CTMC, is highlighted. Finally, artificial geometries of simplified morphologies (samples of identical overlapping semi-transparent spheres with the optical properties of ice) are generated and used for the calculation of the macroscopic optical properties by the Monte Carlo simulation. This allows for an in depth understanding of the influence of the snow morphology and the radiative transfer model (homogenized versus multiphase) on the macroscopic optical properties.

**Table 1.** Grain Shape Classification (ICSSG), Measured Density, and Preparation Method of the Five Characteristic Snow Types

| Symbol | Type | ICSSG | $\rho_{ex}$ ($gcm^{-3}$) | Preparation |
|---|---|---|---|---|
| *ds* | decomposing snow | DFdc | 0.11 ± 0.01 | fresh snow for 8 days at −50°C |
| *mI* | metamorphosed I | RGsr/DFdc | 0.15 ± 0.01 | fresh snow for 14 days at −17°C |
| *mII* | metamorphosed II | RGsr | 0.19 ± 0.05 | fresh snow for 17 days at −3°C |
| *dh* | depth hoar | DHcp | 0.31 ± 0.02 | snow from field |
| *ws* | Wet snow | MFcl | 0.54 ± 0.03 | snow from field, soaked with ice water |

### 3.1. Morphology Characterization

[15] *Computed Tomography* (*CT*). Five characteristic, metamorphosed, natural snow types are considered. These types cover the grain shape classifications DFdc, RGsr/DFdc, RGsr, DHcp and MFcl of the International Classification for Seasonal Snow on the Ground (ICSSG) [*Fierz et al.*, 2009], and have been used in previous studies for the determination of snow's specific surface area [*Kerbrat et al.*, 2008]. Three types of snow, called "decomposing snow" (*ds*), "metamorphosed I" (*mI*) and "metamorphosed II" (*mII*), were prepared by sieving fresh snow after precipitation into boxes at different temperatures, allowing for isothermal metamorphism at different rates. Two additional snow types were collected in the field: "depth hoar" (*dh*) was collected in blocks, and "wet snow" (*ws*) was sieved into boxes and soaked with ice water. Table 1 lists the grain shape classification (ICSSG), measured density, and preparation method of the five characteristic snow types.

[16] Computed tomography is carried out with a Scanco $\mu$CT 80 desktop X-ray with a microfocus X-ray source emitting a polychromatic spectrum at an acceleration voltage of 45 keV. The sample is scanned at 1000 angles over 180°. Each measurement is an average over two scans with exposure times of 0.25 s. The resulting voxel sizes are 10 $\mu$m for *ds*, *mI* and *mII* and 18 $\mu$m for *dh* and *ws.* The CT data is filtered with a median and Gaussian filter (each 3 × 3 × 3) and subsequently segmented by the mode method. Figure 2 shows 3D surface rendering of the five characteristic snow types.

[17] *Porosity, specific surface area, representative elementary volume, pore- and particle-size distributions.* The two-point correlation function is used to calculate porosity, $\varepsilon$, and specific surface area, $A_0$, of the snow samples [*Berryman and Blair*, 1986]. $\varepsilon$ is defined as the volume fraction of the void phase and is equal to $1\text{-}\rho_{snow}/\rho_{ice}$. $A_0$ is defined as air-ice phase boundary surface per snow volume. Good agreement to specific surface area measured for the same samples by gas adsorption [*Kerbrat et al.*, 2008] is observed. The representative elementary volume (REV), the smallest snow volume for which the continuum assumption is still valid, is calculated based on $\varepsilon$ with a tolerance band ±0.05 for cubic subvolume sizes at 20 random locations within the sample. Table 2 lists the calculated and experimentally measured $\varepsilon$ and $A_0$, and the calculated edge length of the cubic REV, $l_{REV}$, for the five characteristic snow types. The mathematical morphology operation opening with a spherical structuring element is applied to calculate the pore- and particle-size distributions, defined as the size distributions of spheres that fit completely within the pore or particle spaces respectively. Figure 3 shows the opening distribution functions of the pores and particle sizes for the five snow types. The mean pore and particle diameters are listed in Table 2. Thus, the assumption of geometrical optics is valid for $\lambda < \pi d_{min}$ = 157 $\mu$m, based on the smallest mean pore and particle diameter calculated.

### 3.2. Particle- and Pore-Level Radiative Properties

[18] In this section, the air phase and the ice particles of the snow are referred to as fluid and solid phases respectively. The corresponding phase indices *i*, *j* used in equations (2)–(6) for the CTMC model are 1 for the fluid phase and 2 for the solid phase. Spectral calculations of the radiative properties are performed at 65 distinct wavelengths between 0.3 $\mu$m and 3 $\mu$m for CTMC and at 150 wavelengths for DISORT. The bulk properties of pure ice are determined based on the complex refractive index of ice, as shown in Figure 4 for 0.3 $\mu$m < $\lambda$ < 3 $\mu$m [*Warren and Brandt*, 2008]. Internal scattering is assumed to be zero neglecting any impurities present in the ice particles. The absorption coefficient is calculated from the imaginary part of the refractive index of ice, $\kappa_2 = 4\pi k/\lambda$, according to electromagnetic theory [*Born and*

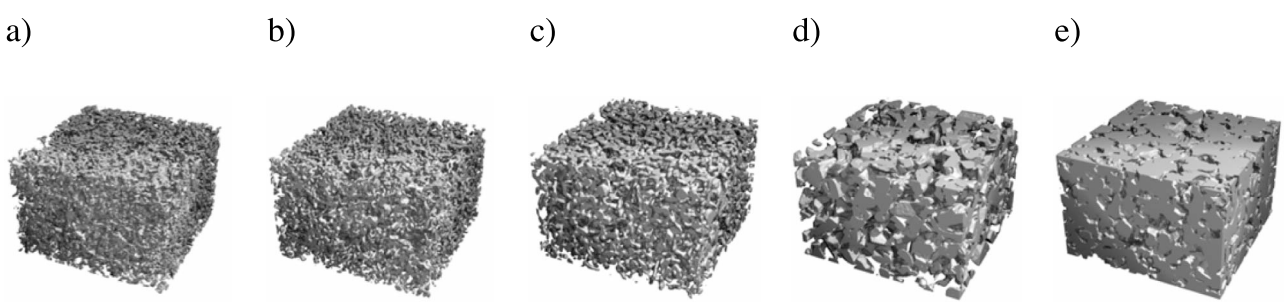


**Figure 2.** 3D surface rendering of the five snow types (Table 1): (a) *ds*, (b) *mI*, (c), *mII*, (d), *dh*, and (e) *ws*. The size of samples from Figures 2a–2c is 6 × 6 × 4 $mm^3$ and the size of samples from Figures 2d and 2e is 10.8 × 10.8 × 7.2 $mm^3$.

**Table 2.** Calculated and Experimentally Measured Porosity and Specific Surface Area, Calculated Edge Length of the Cubic REV, and Mean Pore and Particle Diameter for the Five Characteristic Snow Types

| Type | $\varepsilon$ | $\varepsilon_{ex}$[a] | $A_0$ ($m^{-1}$) | $A_{0,ex}$[a] ($m^{-1}$) | $l_{REV,\gamma=0.05}$ (mm) | $d_{m,pore}$ (mm) | $d_{m,particle}$ (mm) |
|---|---|---|---|---|---|---|---|
| ds | 0.854 | 0.88 ± 0.01 | 8178 | 6776 ± 694 | 0.63 | 0.24 | 0.05 |
| mI | 0.845 | 0.84 ± 0.01 | 6450 | 5190 ± 383 | 1.27 | 0.27 | 0.08 |
| mII | 0.805 | 0.79 ± 0.05 | 5488 | 5130 ± 1473 | 1.37 | 0.32 | 0.13 |
| dh | 0.670 | 0.66 ± 0.02 | 2777 | 2883 ± 242 | 3.33 | 0.75 | 0.40 |
| ws | 0.384 | 0.40 ± 0.03 | 3016 | 2646 ± 219 | 3.93 | 0.41 | 0.66 |

[a]Experimentally measured.

*Wolf*, 1999; *Modest*, 2003]. The fluid phase is assumed to be transparent, i.e., its refractive index is equal to 1 and its internal absorption and scattering coefficients ($\sigma_{s,1}$, $\kappa_1$) are negligible and taken equal to zero as the absorption coefficients of air is orders of magnitude smaller than the extinction of radiation at the solid-fluid boundary, e.g., when calculated based on the HITRAN2004 database [*Rothman*, 2005]. The directional-hemispherical reflectivities at the specular fluid-solid interface for radiation incident from the fluid phase and from the solid phase (including absorption within ice), needed for CTMC, are calculated by the Fresnel's equations [*Born and Wolf*, 1999; *Modest*, 2003].

[19] The scattering coefficients of the five characteristic snow types calculated by CTMC are shown in Figure 5 as a function of wavelength, for the fluid phase (Figures 5a and 5b) and the solid phase (Figures 5c and 5d). For any phase, $\sigma_{s,ij}$ is complementary to $\sigma_{s,refl,i}$ since it refers to the transmitted portions of radiation across the interface. $\sigma_{s,refl,2}$ and $\sigma_{s,21}$ are additionally influenced by the presence of the total reflection phenomenon in the particle. The apparent scattering coefficient of the same snow types calculated by Mie theory is shown in Figure 5e.

[20] The corresponding extinction coefficients $\beta_i$ are shown in Figure 6. As expected, $\beta_1$ calculated by CTMC is independent of $\lambda$ because it is a function of the interface geometry only. For $\lambda > 1.5$ $\mu$m, the influence of internal absorption in the ice (described by $\kappa_2$) becomes relevant to $\sigma_{s,refl,2}$ and $\sigma_{s,21}$. Therefore, $\beta_2$ calculated by CTMC increases with $\lambda$, following qualitatively the $\lambda$-dependence of $\kappa_2$. For $\lambda > 2.7$ $\mu$m, internal absorption strongly increases and leads to the blackbody-like behavior of ice in the NIR spectral region. The apparent extinction coefficient, calculated by Mie theory, is nearly independent of $\lambda$.

[21] Figure 7 shows the scattering phase functions as a function of the cosine of the scattering angle, $\mu_s$, for the five characteristic snow types calculated by CTMC at $\lambda$ = 0.5 $\mu$m (a) and at $\lambda$ = 1.5 $\mu$m (b), the apparent scattering phase function calculated by Mie theory at $\lambda$ = 0.5 (c) and $\lambda$ = 1.5 $\mu$m (d), and the asymmetry factor as function of wavelength (e). For CTMC, the scattering phase functions behave nearly identical for the five characteristic snow samples while no significant wavelength dependence is observed, which is consistent with the low sensitivity of the two-phase medium scattering functions on morphology [*Haussener et al.*, 2010a; *Tancrez and Taine*, 2004]. The sharp increase in $\Phi_{ref,2}$ is explained by the total reflection phenomena leading to an increased fraction of forward scattering. The phase functions calculated by Mie theory, shown in Figures 7c and 7d, do not exhibit significant dependence on wavelength, while the influence of the snow type can be practically neglected. The asymmetry factor $g$ shows both wavelength-dependence and variations due to snow type at

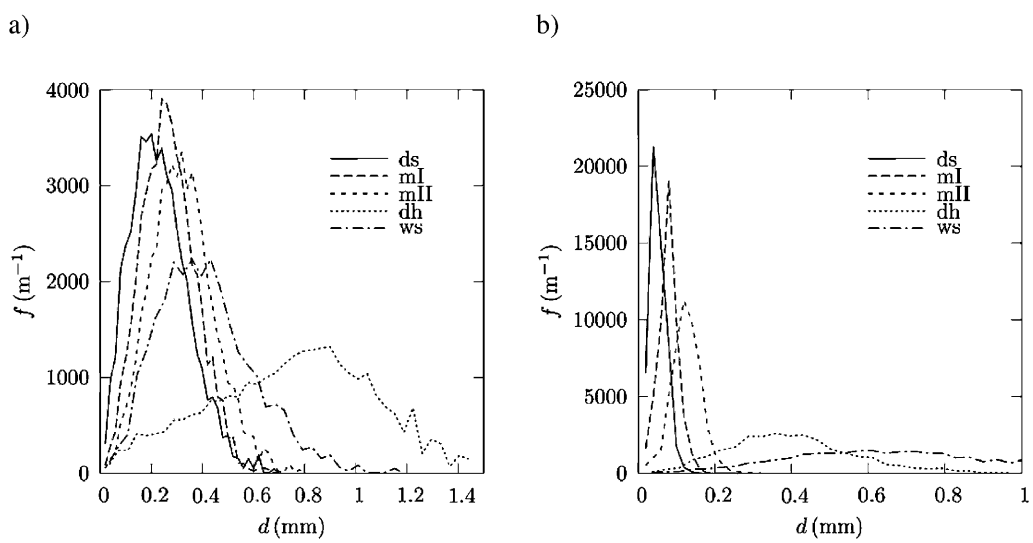


**Figure 3.** Opening size distribution functions of (a) the pores and (b) the particles for the five characteristic snow types (Table 1).

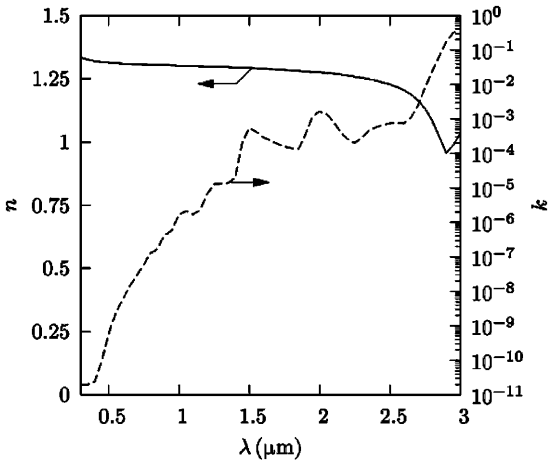


**Figure 4.** Real (solid line) and imaginary (dotted line) part of the complex refractive index of ice.

$1.5 < \lambda < 2.75$ $\mu$m. An increase in $g$ corresponds to a larger fraction of forward scattering. Snow types with smaller $A_0$ exhibit enhanced forward scattering.

### 3.3. Macroscopic Optical Snow Properties

[22] Figures 8a and 8b show the spectral reflectance and transmittance respectively of the five characteristic snow types as a function of wavelength, calculated by CTMC for a snow slab of thickness $l_{\mathrm{slab}} = 4$ cm and for collimated incident radiative flux. Figures 8c and 8d show the corresponding curves for diffuse incident radiative flux. As expected, $R$ increases and $Tr$ decreases for incident diffuse radiation. For example, for *ws*, $R$ increases by up to 15% while $Tr$ decreases by up to 35% for $\lambda < 1$ $\mu$m. All curves follow the $\lambda$-dependence of $\kappa_2$. The results are qualitatively in agreement with the radiative properties of snow with varying spherical grain radius [*Wiscombe and Warren*, 1980]. The normalized differences of $R$ and $Tr$ calculated by DISORT and CTMC are shown as a function of wavelength in Figures 9a and 9b, respectively, for collimated incident radiation, and in Figures 9c and 9d, respectively, for diffuse incident radiative. For collimated incident radiation at $\lambda < 1$ $\mu$m, $R$ differs by maximal 20% (for *ws*) while $Tr$ differs by up to 121% (for *mI*). For most of the snow types the difference increases at longer wavelength due to the smaller absolute values of $R$ and $Tr$. DISORT-based calculations differ from CTMC-based calculations for diffuse incident radiation by maximal 16% (for *ws*) in $R$ and by up to 121% (for *mI*) in $Tr$ for $\lambda < 1$ $\mu$m. Therefore, the difference in the calculated $R$ and $Tr$ based on CTMC or DISORT are not caused by the radiative boundary condition (i.e., collimated versus diffuse) but rather by the simplified snow morphologies and the inherently different approaches to model radiative transfer.

[23] The best agreement for $R$ between both models is observed for *ds*, while *dh* and *ws* exhibit large differences. This is expected as the assumption of homogeneous scattering medium consisting of spheres is not applicable for the coarse directional structures of *dh* and the assumption of a dilute collection of independently scattering spheres is not applicable to the low porosity *ws*. The best agreement for $Tr$ between both models is observed for *ds*, while *mI* and *mII* – consisting of nearly spherically shaped grains and high porosity – shows, surprisingly, the largest difference. This discrepancy is not due to the break-down of the DISORT assumptions but due to differences in the calculated effective/apparent radiative properties, which are highly sensitive to the morphology, which cannot easily by described by only two morphological characteristics (e.g., $\varepsilon$ and $A_0$, which are themself difficult to determine). As the effective/apparent radiative properties are more crucial for the determination of $Tr$ the agreement pattern between CTMC and DISORT is different for $Tr$ and $R$.

[24] *Simplified geometries.* Monte Carlo ray-tracing, as applied in the second step of the CTMC model for solving two coupled RTEs (equation (2), Section 2.1), is applied to simplified equivalent snow morphologies (idealized geometries). Results are compared to those obtained by CTMC and DISORT to elucidate the effect of (*i*) simplifying the geometry versus incorporating the CT-determined snow microstructure, and (*ii*) solving one homogenized RTE, equation (7), versus two coupled, multiphase RTEs, equation (2). The simplified geometry consists of an artificially generated regularly structured packed bed composed of identical overlapping semi-transparent spheres (IOSS). Porosity, $\varepsilon_{\mathrm{IOSS}}$, and specific surface area, $A_{0,\mathrm{IOSS}}$, of IOSS are given by *Tancrez and Taine* [2004]:

$$\varepsilon_{\mathrm{IOSS}} = \exp\left(-n_V d^3 \frac{\pi}{6}\right), \tag{12}$$

$$A_{0,\mathrm{IOSS}} = -\frac{6\varepsilon_{\mathrm{IOSS}} \ln(\varepsilon_{\mathrm{IOSS}})}{d}, \tag{13}$$

where $n_V$ describes the number of spheres per volume and $d$ the diameter of the identical spheres. Three types of IOOS samples are generated: (*i*) $d = d_{\mathrm{m}}$ and $\varepsilon_{\mathrm{IOSS}} = \varepsilon$; (*ii*) $A_{0,\mathrm{IOSS}} = A_0$ and $\varepsilon_{\mathrm{IOSS}} = \varepsilon$; and (*iii*) $d = d_{\mathrm{m}}$ and $A_{0,\mathrm{IOSS}} = A_0$, with $A_0$, $\varepsilon$ and $d_{\mathrm{m}}$ given in Table 2 for each snow type.

[25] Figure 10 shows $R$ (Figures 10a and 10b) and $Tr$ (Figures 10c and 10d) of a slab of $l_{\mathrm{slab}} = 4$ cm for *ds* (Figures 10a and 10c) and *ws* (Figures 10b and 10d) calculated by the CTMC model, by Monte Carlo for idealized geometries with 3 types of IOSS, and by DISORT. Table 3 lists the normalized 2-norm, $\xi$ (equations (14) and (15)), of $R$ and $Tr$ for the five characteristic snow types calculated by CTMC, by Monte Carlo for idealized geometries with 3 types of IOSS, and by DISORT. The relative difference of $R$ and $Tr$ for the five characteristic snow types calculated by CTMC, by Monte Carlo for idealized geometries with 3 types of IOSS, and by DISORT at wavelengths used by spectroradiometers of satellites or by remote sensing tools ($\lambda = 0.5$, 0.85, 1, 1.3, and 1.5 $\mu$m) are listed in the Appendix A.

$$\xi_R = \frac{\left\| R_{\mathrm{IOSS,type}_i} - R_{\mathrm{CT/DIOSRT}} \right\|}{\left\| R_{\mathrm{CT/DIOSRT}} \right\|} \tag{14}$$

$$\xi_{Tr} = \frac{\left\| Tr_{\mathrm{IOSS,type}_i} - Tr_{\mathrm{CT/DIOSRT}} \right\|}{\left\| Tr_{\mathrm{CT/DIOSRT}} \right\|} \tag{15}$$

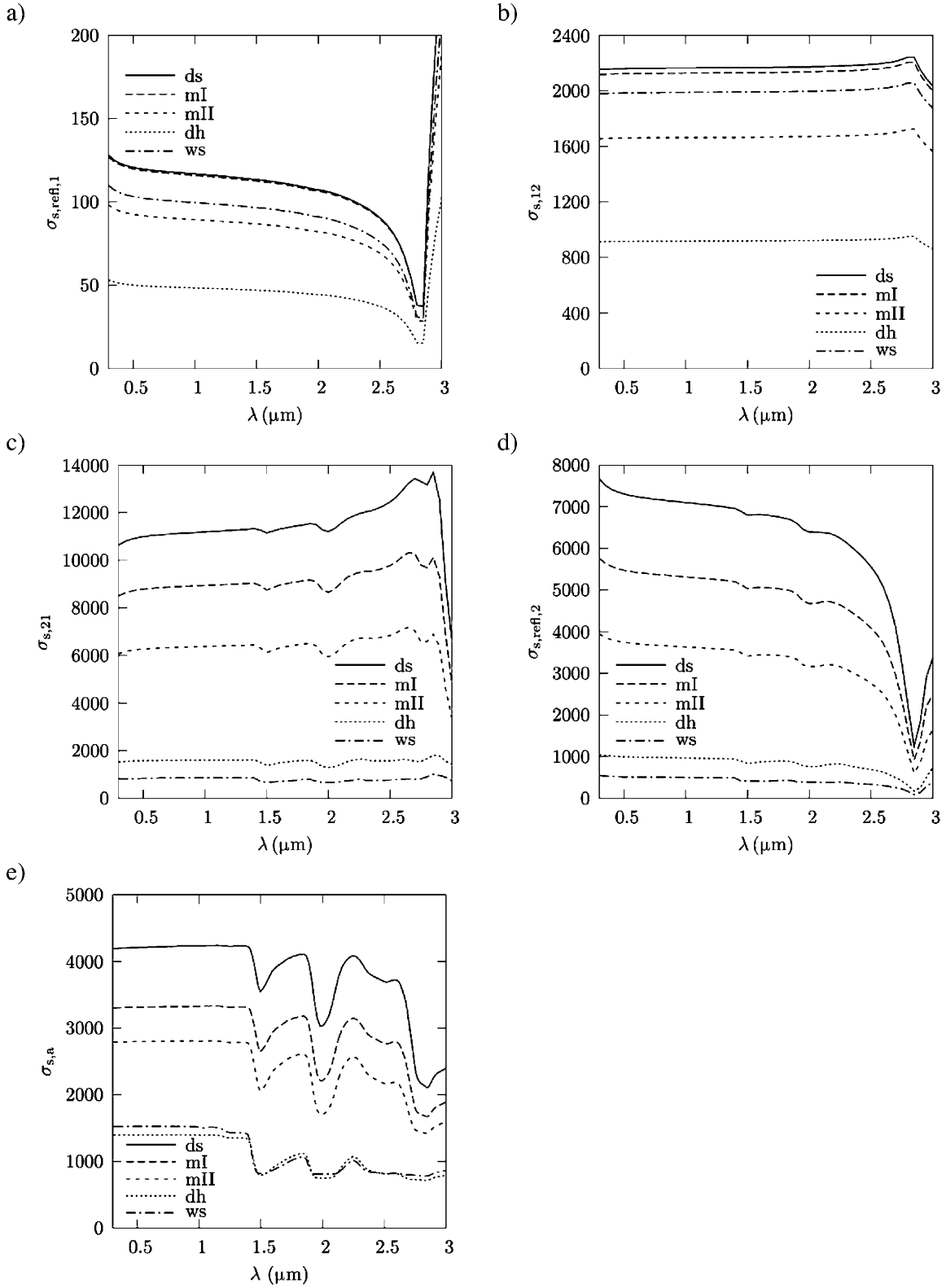


**Figure 5.** Spectral scattering coefficients of the five characteristic snow types for (a, b) the fluid phase and (c, d) the solid phase calculated by CTMC, and (e) the apparent scattering coefficient calculated by Mie theory.

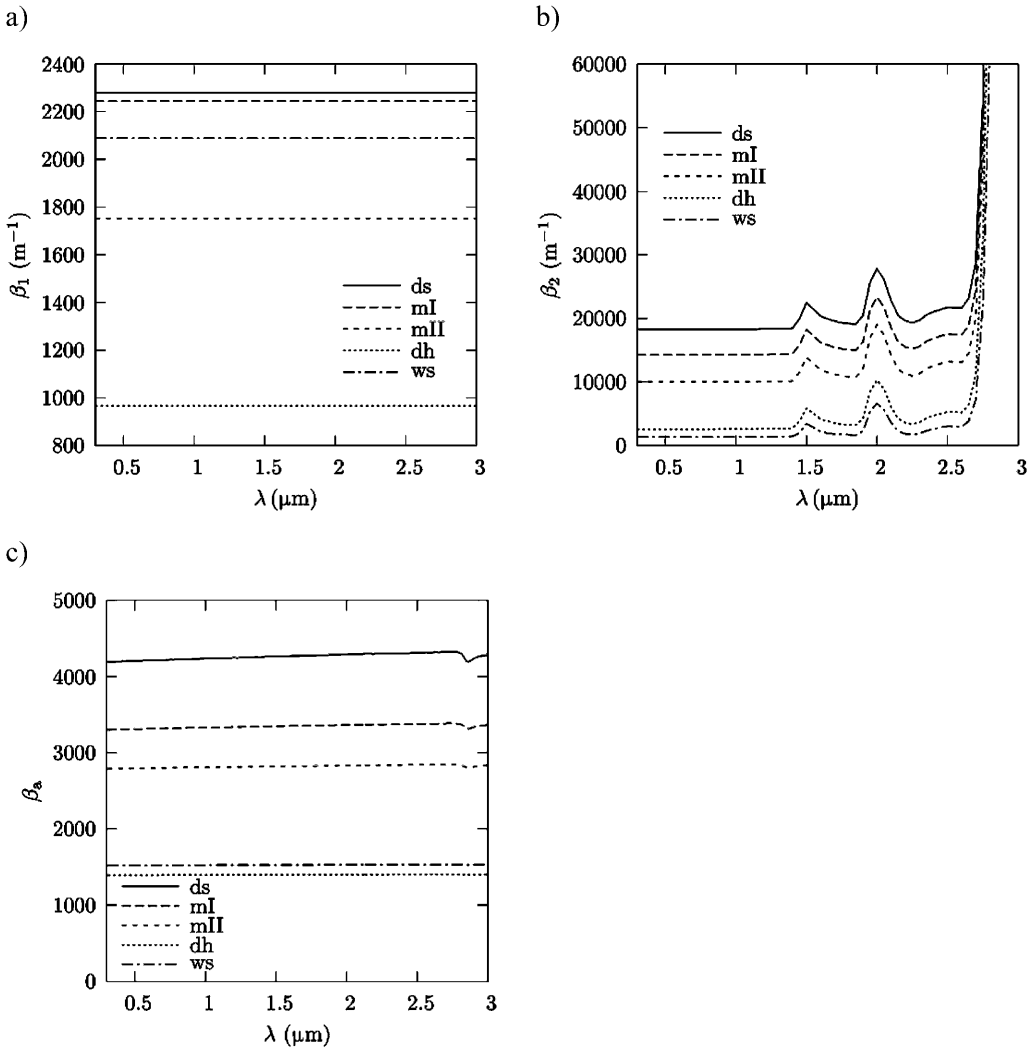


**Figure 6.** Spectral extinction coefficients of the five characteristic snow types for the (a) fluid phase and (b) solid phase calculated by CTMC, and the (c) apparent extinction coefficient calculated by Mie theory.

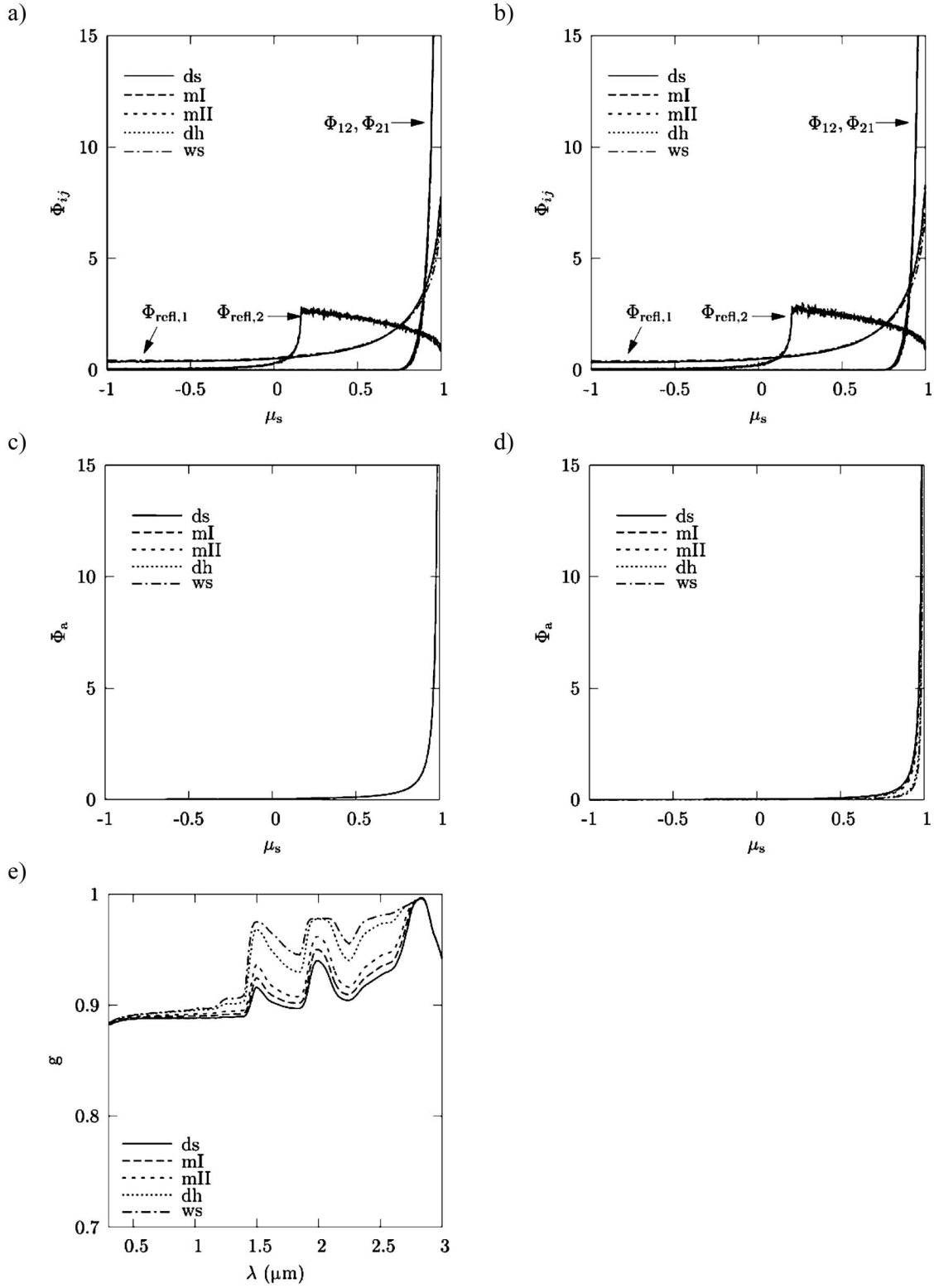


**Figure 7.** Scattering phase functions as a function of the cosine of the scattering angle for the five characteristic snow types calculated by CTMC at (a) $\lambda = 0.5$ $\mu$m and (b) $\lambda = 1.5$ $\mu$m, the apparent scattering phase function calculated by Mie theory at (c) $\lambda = 0.5$ and (d) $\lambda = 1.5$ $\mu$m, and (e) the asymmetry factor as a function of wavelength.

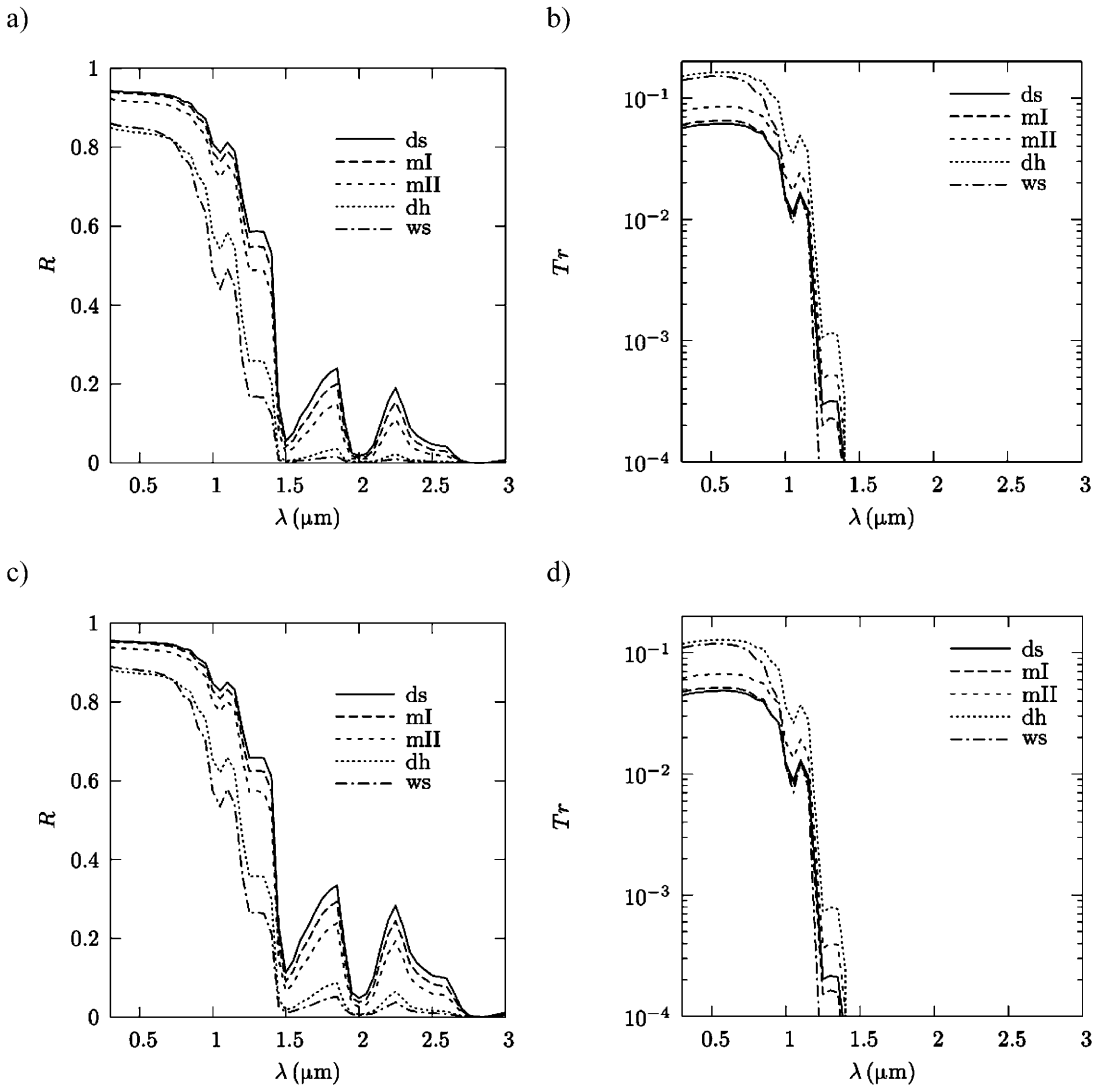


**Figure 8.** (a, c) Spectral reflectance and (b, d) transmittance of the five characteristic snow types calculated by CTMC for a snow slab of thickness $l_{slab}$ = 4 cm and for collimated incident radiation flux (Figures 8a and 8b) and diffuse incident radiative flux (Figures 8c and 8d).

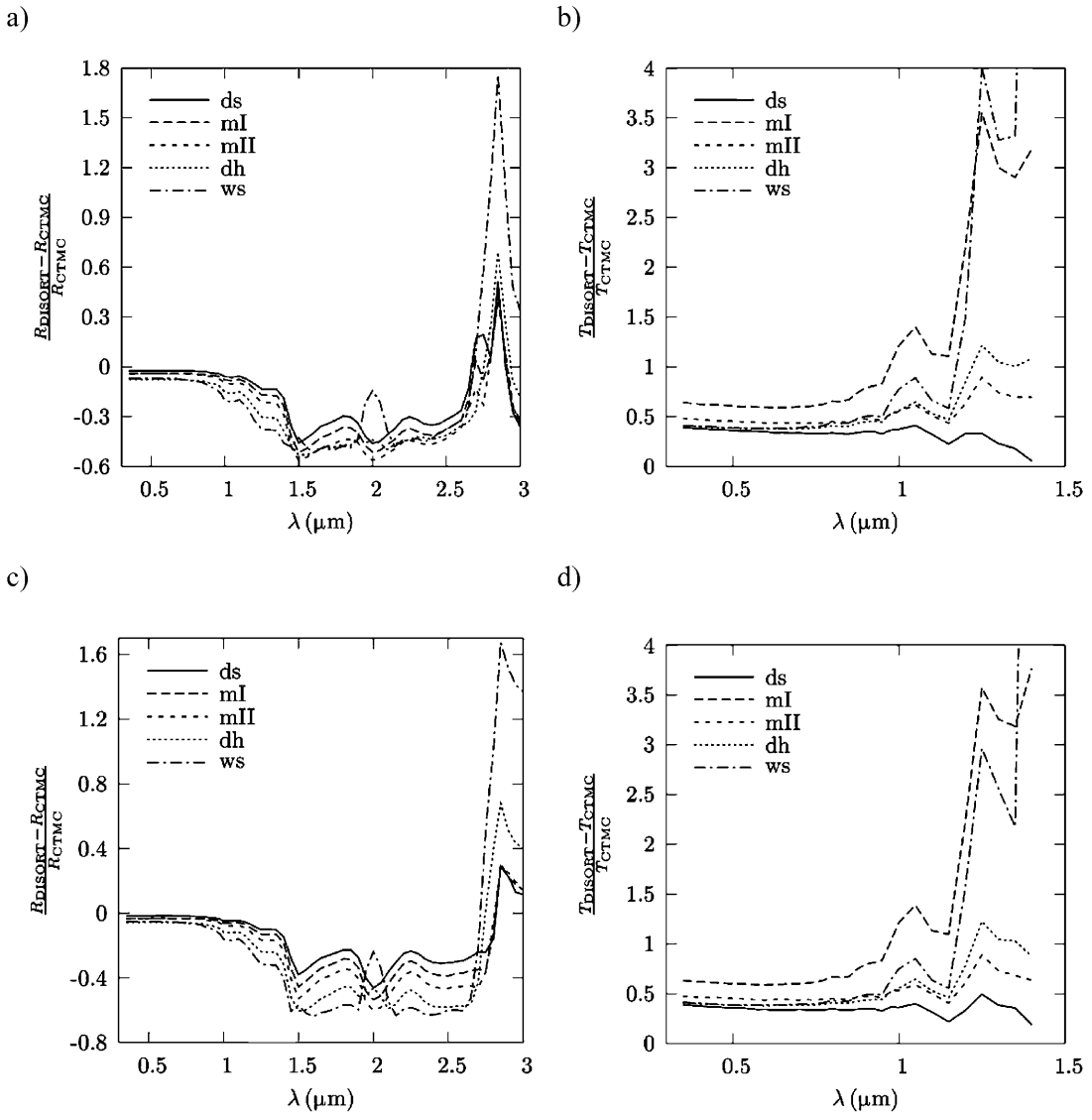


**Figure 9.** Normalized difference of the (a, c) reflectance and (b, d) transmittance between the calculated values by DISORT and CTMC for the five characteristic snow types for collimated incident radiation flux (Figures 9a and 9b) and diffuse incident radiative flux (Figures 9c and 9d).

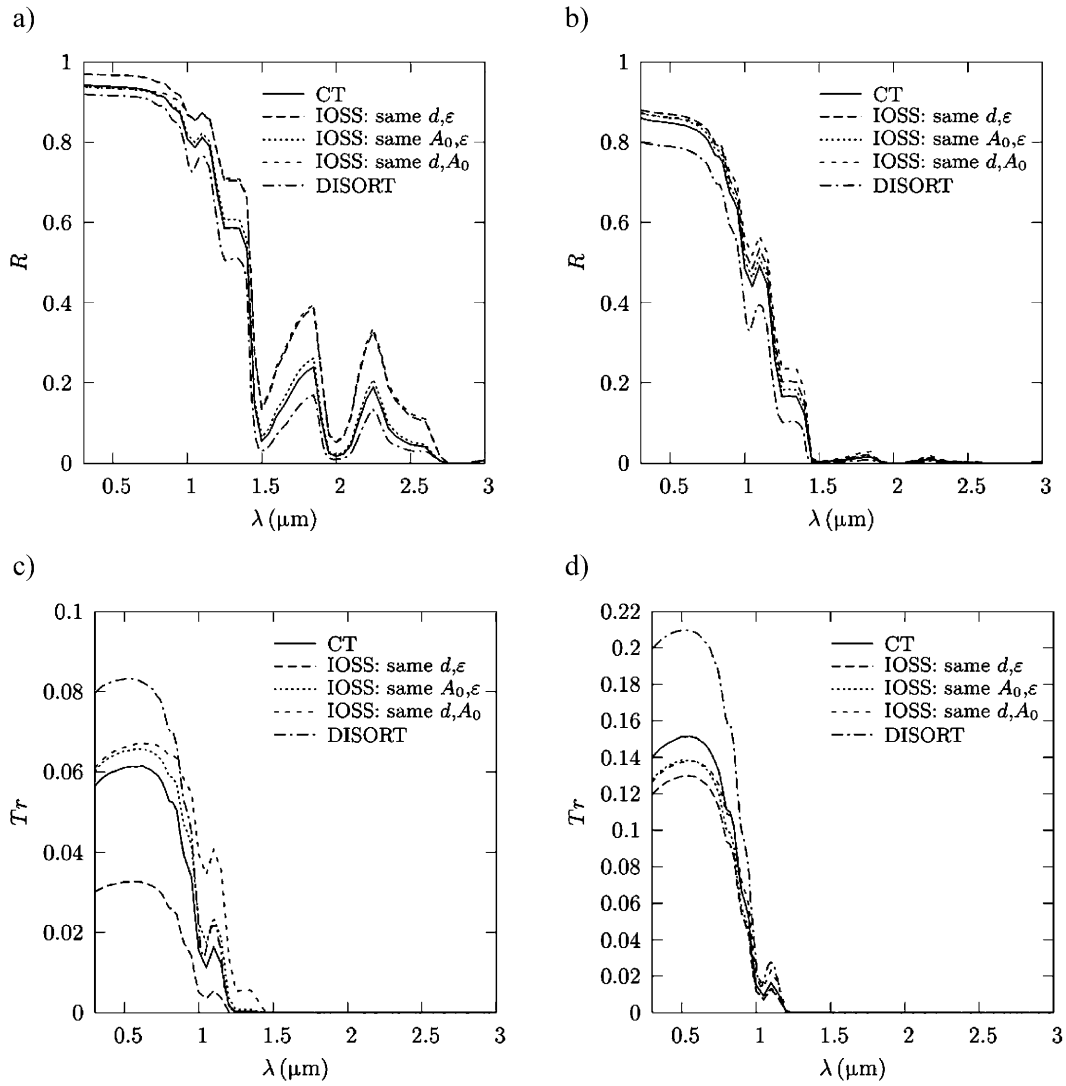


**Figure 10.** (a, b) Reflectance and (c, d) transmittance of a snow slab of $l_{\text{slab}}$ = 4 cm for snow types *ds* (Figures 10a and 10c) and *ws* (Figures 10b and 10d) calculated by the CTMC, by Monte Carlo for idealized geometries with 3 types of IOSS, and by DISORT.

**Table 3.** Normalized 2-norm, $\xi$, of $R$ and $Tr$ for the Five Characteristic Snow Types Calculated by the CTMC Model, by Monte Carlo for Idealized Geometries With 3 Types of IOSS, and by the DISORT Model

| | CTMC Versus $d_m/\varepsilon$-IOSS | | CTMC Versus $A_0/\varepsilon$-IOSS | | CTMC Versus $d_m/A_0$-IOSS | | DISORT Versus $A_0/\varepsilon$-IOSS | | CTMC Versus DISORT | |
|---|---|---|---|---|---|---|---|---|---|---|
| | $\xi_R$ | $\xi_{Tr}$ | $\xi_R$ | $\xi_{Tr}$ | $\xi_R$ | $\xi_{Tr}$ | $\xi_R$ | $\xi_{Tr}$ | $\xi_R$ | $\xi_{Tr}$ |
| ds | 0.124 | 0.489 | 0.018 | 0.112 | 0.127 | 0.277 | 0.084 | 0.193 | 0.064 | 0.061 |
| mI | 0.083 | 0.228 | 0.019 | 0.313 | 0.087 | 0.492 | 0.092 | 0.214 | 0.077 | 0.292 |
| mII | 0.061 | 0.245 | 0.009 | 0.140 | 0.061 | 0.259 | 0.092 | 0.223 | 0.083 | 0.140 |
| dh | 0.086 | 0.301 | 0.016 | 0.051 | 0.074 | 0.193 | 0.129 | 0.321 | 0.101 | 0.097 |
| ws | 0.044 | 0.149 | 0.022 | 0.092 | 0.068 | 0.082 | 0.139 | 0.353 | 0.104 | 0.102 |

Calculations of $R$ show that IOSS with $A_{0,\mathrm{IOSS}} = A_0$ and $\varepsilon_{\mathrm{IOSS}} = \varepsilon$ best approximate the snow morphology across the entire spectrum for all five snow types. The biggest deviation of $R$ is found for a slab of *ds* ($\xi_R = 0.13$) for IOSS with $A_{0,\mathrm{IOSS}} = A_0$ and $d = d_m$. Nevertheless, using IOSS with $A_{0,\mathrm{IOSS}} = A_0$ and $\varepsilon_{\mathrm{IOSS}} = \varepsilon$ significantly reduces the deviation to $\xi_R = 0.02$, which is comparable to deviations for all other snow types at this best fitting equivalent snow morphology. Although IOSS with $A_{0,\mathrm{IOSS}} = A_0$ and $\varepsilon_{\mathrm{IOSS}} = \varepsilon$ generally approximates well the complex snow structure, $R$ deviations of 6% for *mII* and of 20% for *ws* at $\lambda = 1$ $\mu$m are observed. For $Tr$ calculations, generally much higher $\xi$ are observed since the absolute values of $Tr$ are lower, especially at large $\lambda$. The best fitting equivalent morphology for $Tr$ is IOSS with $A_{0,\mathrm{IOSS}} = A_0$ and $\varepsilon_{\mathrm{IOSS}} = \varepsilon$. Only for *mI*, IOSS with $d = d_m$ and $\varepsilon_{\mathrm{IOSS}} = \varepsilon$ and for *ws*, IOSS with $d = d_m$ and $A_{0,\mathrm{IOSS}} = A_0$, respectively, better approximates the true snow morphology. $Tr$ for *mI* and *mII* yield larger deviations than those for the denser *dh* and *ws*. $Tr$ for a slab of *mI* is worst approximated by IOSS with $A_{0,\mathrm{IOSS}} = A_0$ and $\varepsilon_{\mathrm{IOSS}} = \varepsilon$ ($\xi_{Tr} = 0.32$), while a slab of *dh* is best approximated ($\xi = 0.05$). Nevertheless, $Tr$ deviates by e.g., 6% for *dh* and by 116% for *mI* at $\lambda = 1$ $\mu$m.

[26] Solving one homogenized RTE (equation (7), by DISORT) instead of two coupled, multiphase RTEs (equation (2), by CTMC and by Monte Carlo with IOSS) generally leads to lower $R$. This is seen for example for *ws*, where the difference is up to $\xi_R = 0.14$ between DISORT and IOSS with same $A_0$ and $\varepsilon$. In general, the difference between DISORT and IOSS with same $A_0$ and $\varepsilon$ increases with decreasing porosity. For *ws*, the difference between the CTMC model and IOSS with same $A_0$ and $\varepsilon$ is only $\xi_R = 0.02$ and $\xi_R = 0.10$ between CTMC and DISORT. We conclude that DISORT's lower $R$ values are mainly due to simplifications in the radiative transfer model than due to simplifications in the snow morphology ($\xi_{R,\mathrm{DISORT}\text{-}A0/\varepsilon\text{-IOOS}} \gg \xi_{R,\mathrm{CT}\text{-}A0/\varepsilon\text{-IOOS}}$). The latter accounts for 10–21% of the difference in $R$.

[27] $Tr$ calculated by DIOSRT is larger. This is seen for example for *ws*, where the difference is up to $\xi_{Tr} = 0.35$ between DISORT and IOSS with same $A_0$ and $\varepsilon$ (and decreasing for snow types with higher porosity), while it is only $\xi_{Tr} = 0.09$ between CTMC and IOSS with same $A_0$ and $\varepsilon$. For *ws*, $\xi_{Tr} = 0.55$ between CTMC and DISORT. We conclude that DISORT's larger $Tr$ values are due to simplification in the snow morphology as well as to simplification in the radiative transfer model ($\xi_{Tr,\mathrm{DISORT}\text{-}A0/\varepsilon\text{-IOOS}} \approx \xi_{Tr,\mathrm{CT}\text{-}A0/\varepsilon\text{-IOOS}}$). Simplification in morphology accounts for 16–146% of the difference in $Tr$.

### 3.4. Discrete-Scale Radiative Heat Transfer Analysis

[28] In addition to the determination of the macroscopic optical properties based on the exact snow morphology, CTMC allows - in contrast to the spatially homogeneous DISORT - for an in-depth heat transfer analysis on the exact microstructure based on direct numerical simulations at the pore-level scale. The exact location of radiation scattering, emission and absorption is of interest for snow recrystallization. Weak layers, which are the most common cause of snow avalanches, are mainly formed at or very close to the snow surface. The formation and recrystallization of such layers is not yet well understood, and the spectral and morphological-dependence of the absorption and scattering characteristics may play an important role in this process.

[29] As an example, the absorbed radiation in the *xy*-plane at $z = 0.2$ mm within a $6 \times 6 \times 4$ mm$^3$ *mII* sample and a $10.8 \times 10.8 \times 7.2$ mm$^3$ *ws* sample, respectively, irradiated with diffuse radiation at $z = 0$ and black surrounding for the other five walls is depicted in Figure 11 for $\lambda = 1$ and 2.5 $\mu$m. Radiation is predominantly absorbed near the surface of the ice particle. At $\lambda = 2.5$ $\mu$m, internal absorption within ice is two orders of magnitude larger (see Figure 4) and, therefore, more radiative energy is absorbed in the ice matrix. In addition, the effective (volumetric) radiative properties determined by CTMC allow for a statistical and spatial averaged investigation of radiative heat transfer at the pore-level scale, shown in Figure 11f for *mII* at $\lambda = 1$ $\mu$m, with significant savings in computational expenses [*Petrasch et al.*, 2011]. The volumetric absorption within *mII* and *ws* samples is depicted in Figure 12 for $\lambda = 2.5$ $\mu$m. Radiation is predominantly absorbed in a thin surface layer of the snow and at the surface of the grains.

## 4. Comparison to Transmittance Measurements

[30] Transmittance measurements of different snow samples are performed and compared to calculated transmittance to validate the different modeling approaches. An integrating sphere setup is used utilizing a 60 W halogen lamp as radiation source [*Gergely et al.*, 2010]. Diffuse radiation incident on the snow sample with cross-sectional area $20 \times 20$ cm$^2$ and of thickness $l_{\mathrm{slab}}$ (between 2 and 5 cm) is transmitted and detected by a VNIR FieldSpec Pro spectrometer (Analytical Spectral Devices) with 3° field of view in the 0.35–1.05 $\mu$m spectral region. The chosen sample dimensions and the fact that the samples are larger than the illumination area allow for minimizing the boundary effects on the results [*Beaglehole et al.*, 1998], keeping the transmittance signal high, keeping

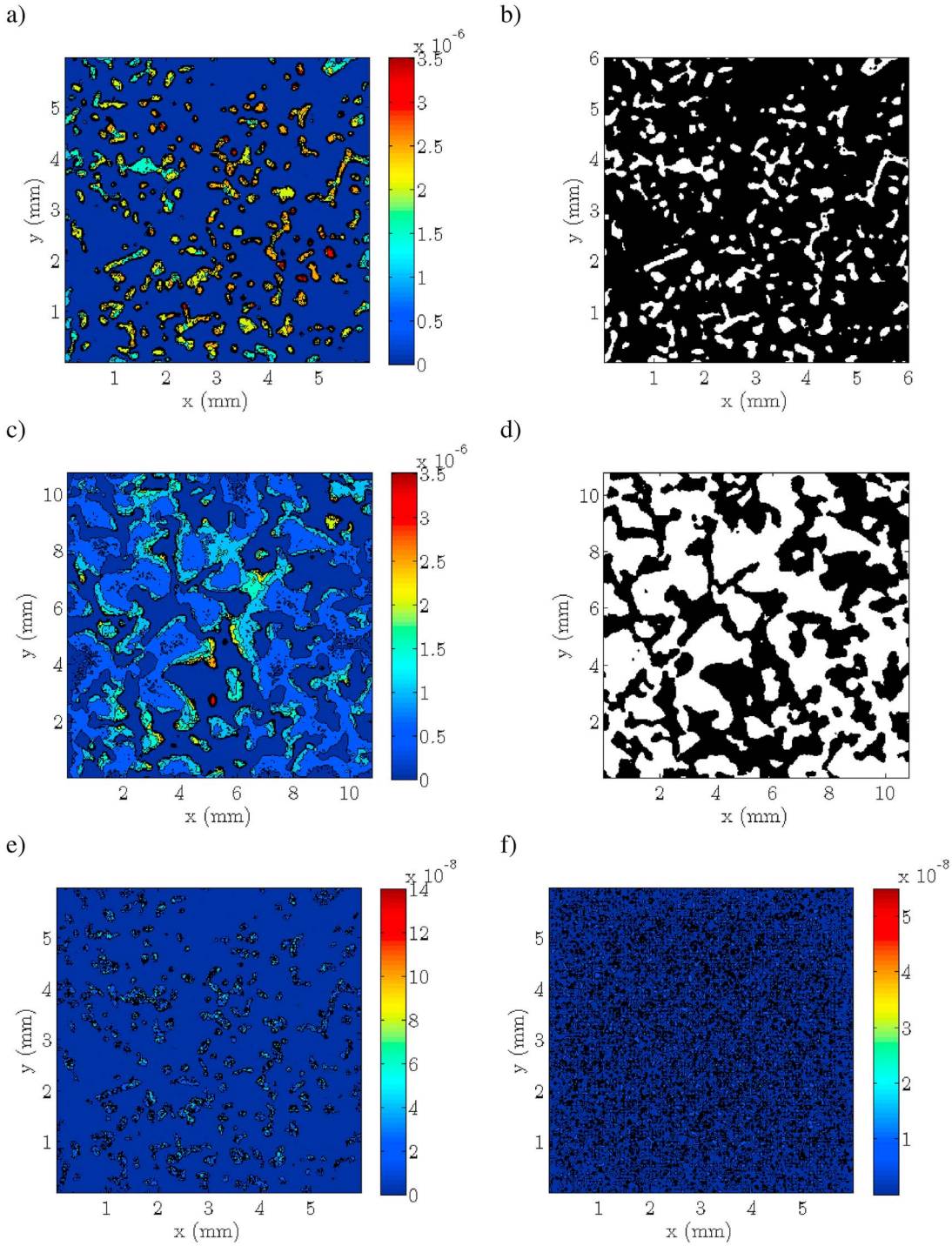


**Figure 11.** Fraction of incident energy absorbed ($q_a/q_{in}$) at the pore-level scale in the *xy*-plane ($z$ = 0.2 mm) of the (a, e) *mII* type snow and the (c) *ws* snow type, for $\lambda$ = 1 $\mu$m (Figure 11e) and 2.5 $\mu$m (Figures 11a and 11c). (b, d) The corresponding snow structure is shown, where black denotes void/air phase and white the ice particle. (f) The statistically and spatial averaged absorption behavior in *mII* snow type for $\lambda$ = 1 $\mu$m at $z$ = 0.2 mm is depicted.

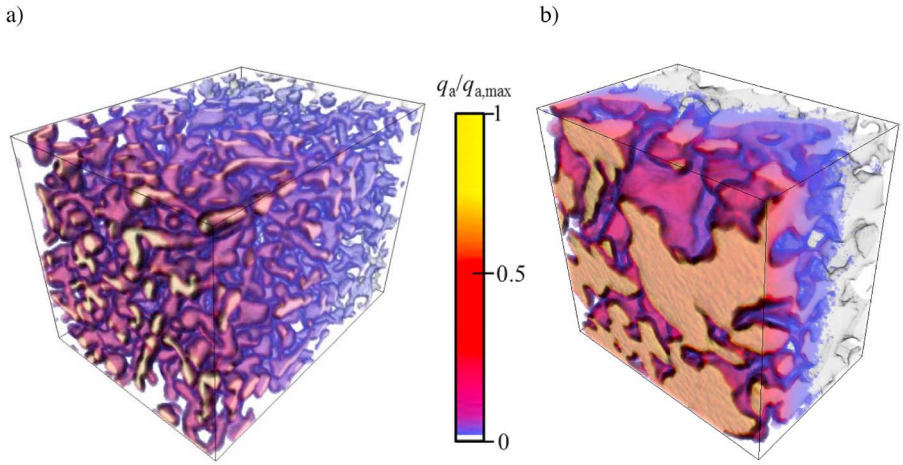


**Figure 12.** Fraction of energy absorbed to maximal energy absorbed ($q_a/q_{a,max}$) at the pore-level scale in a (a) $3 \times 3 \times 4$ mm$^3$ *mII* type and a (b) $5.4 \times 5.4 \times 7.2$ mm$^3$ *ws* type snow sample at $\lambda = 2.5$ $\mu$m. The samples are diffusely irradiated from the front.

the illuminated area representative of the snow structure while maintaining uniform and diffuse illumination over the whole sample. The sphere itself is made of Styrofoam with an interior coating of aluminum foil, spray-painted in flat white minimizing rays exiting the sphere without reflection and therefor allows for a nearly perfect uniform and diffuse sample illumination. DISORT and CTMC both neglect any effects due to finite sample dimensions perpendicular to the direction of the incident radiation and finite illuminated snow sample area.

[31] Samples of seven additional snow types are investigated: small melt forms "*mf*," small rounded grains "*rg*," fine-grained machine made "*mm*," decomposing and fragmented precipitation particles "*def*" and "*defII*," depth hoar "*deh*," and small rounded grains and facetted snow crystals "*rf*." Their morphological characterization is given in Table 4 and their 3D surface rendered geometry is shown in Figure 13. After the transmittance measurements, three subsamples of each snow type are scanned by the CT setup described in section 3.1, with a voxel size of 10 $\mu$m to 18 $\mu$m. The CT scans are used for transmittance calculations by CTMC and DISORT, as described in sections 2.1 and 2.2 respectively. Figure 14 shows the experimentally measured transmittance for the three types of snow at $\lambda = 0.830$ and 0.927 $\mu$m and the numerically calculated values by CTMC and DISORT. The error bars in the calculated values account for the variation of $\varepsilon_{CT}$, $A_{0,CT}$, and $l_{slab}$ between the three subsamples. Reasonable agreement is observed between measured and calculated transmittance values by DISORT at both NIR wavelengths, except for *mm* and *rg* where DISORT based *Tr* is noticeable larger than the experimental results. This is explained by the fact that *mm* is mainly composed of directional thin ice plates at relatively low porosities (this is also true for *rg*) and, therefore, the assumption of particulate media composed of independent scattering spherical particles breaks down. CTMC shows a lower sensitivity to wavelength than DISORT. CTMC shows reasonable agreement between measurements and calculations for *rg* and *mm* but noticeable lower *Tr* values for *deh*. Similarly, CTMC based *Tr* for *mf*, *def*, *defII* and *rf* samples is lower than the measured values at the shorter wavelength ($\lambda = 830$ $\mu$m). This might be a result of the experimentally investigated sample length, which might be not large enough to be representative and, therefore, not enough absorbing ice matrix is present. CTMC shows reasonable agreement at the longer wavelength ($\lambda = 927$ $\mu$m) for the snow types *mf*, *def*, *defII* and *rf*. The discrepancies between the CTMC and the experimentally estimated transmittance also result from the two simplifications of the heat transfer model, namely, assumed geometrical optics (especially for the snow samples with small ice grains or at lower wavelengths) and independent scattering (especially for snow samples with low porosities).

## 5. Summary and Conclusions

[32] A multiscale methodology based on computed tomography and Monte Carlo ray tracing technique, referred to as CTMC, was developed for the determination of the spectrally

**Table 4.** Porosity, $\varepsilon$, Specific Surface Area, $A_0$, and Thickness, $l_{slab}$, of the Three Types of Snow Used for Transmittance Measurements[a]

| Symbol | Sample | $\bar{\varepsilon}$ | $\varepsilon_{CT}$ | $\bar{A}_0$ (m$^{-1}$) | $A_{0,CT}$ (m$^{-1}$) | $l_{slab}$ (cm) |
|---|---|---|---|---|---|---|
| mf | small melt forms | 0.44 | 0.39–0.51 | 8619 | 6500–8400 | 4.0–5.0 |
| rg | small rounded grains | 0.62 | 0.59–0.66 | 5462 | 4800–6100 | 4.7–5.0 |
| mm | fine-grained machine made | 0.67 | 0.67–0.70 | 7742 | 7400–7800 | 4.5–5.0 |
| def | decomposing and fragmented precipitation particles | 0.90 | 0.88–0.90 | 4141 | 3667–4816 | 2.0–3.0 |
| defII | decomposing and fragmented precipitation particles | 0.85 | 0.84–0.85 | 5779 | 5251–5940 | 2.5–3.5 |
| deh | depth hoar | 0.61 | 0.50–0.63 | 3432 | 3021–3296 | 2.5–3.5 |
| rf | small rounded grains and facetted snow crystals | 0.70 | 0.67–0.76 | 5691 | 4070–5927 | 2.5–3.0 |

[a]Calculated mean value is given for 3 subsamples of each type, measured minimum and maximum values are given for six subsamples of each type.

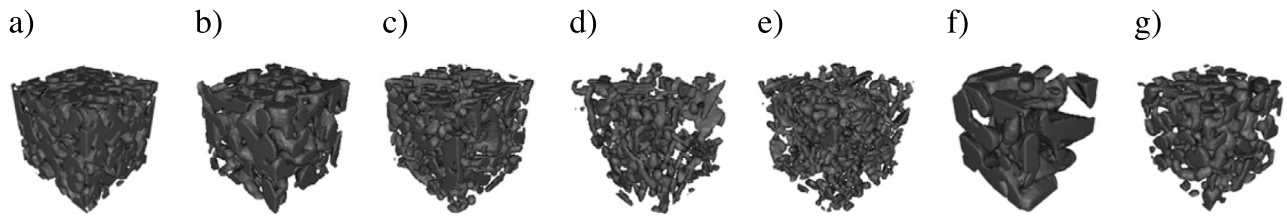


**Figure 13.** 3D surface rendering of the seven snow types of Table 4 used for transmittance measurements: (a) *mf*, (b) *rg*, (c) *mm*, (d) *def*, (e) *defII*, (f) *deh*, and (g) *rf*. The size of the samples is $2 \times 2 \times 2$ mm$^3$.

resolved (0.3–3 $\mu$m) reflectance and transmittance of snow. The complex microstructure of five characteristics snow types was digitalized by computed tomography and used in direct pore-level simulations for the determination of the morphological and effective radiative properties, namely: porosity, specific surface, pore- and particle-size distribution, edge length of the representative elementary volume, extinction coefficients, scattering coefficients, and scattering phase functions. The volume-averaged (continuum) radiation heat transfer model is then applied to determine the overall reflectance, absorptance and transmittance of snow slabs. The model was experimentally validated with transmittance measurements.

[33] The effect of simplifying the snow morphology and the radiative transfer model, i.e., homogenized versus multiphase approach, is examined by comparing CTMC with the widely used DISORT and with a multiphase Monte Carlo model on identically overlapping semitransparent spheres (IOSS). Quantitative differences in radiation behavior resulting from using simplified snow structures and radiative transfer models are reported. Neglecting the exact snow microstructure (CTMC versus MC on IOSS) leads to significant differences in reflectance (up to 4%) and transmittance (up to 116%) for wavelengths smaller than 1 $\mu$m. For most samples, porosity and specific surface area are the most important microstructural characteristics (out of porosity, specific surface area, and grain diameter). IOSS with same porosity and specific surface area approximates best the real snow morphology, yielding $\xi_R = 0.01$ (*mII*) to 0.02 (*ws*), and $\xi_{Tr} = 0.05$ (*dh*) to 0.31 (*mI*). Solving one homogenized RTE with apparent radiative properties instead of two coupled, multiphase RTEs (DISORT versus MC on IOSS) generally leads to lower reflectance values (up to $\xi_R = 0.19$ and 30% difference for $\lambda < 1$ $\mu$m) and larger transmittance values (up to $\xi_{Tr} = 0.35$ and 53% difference for $\lambda < 1$ $\mu$m). The difference of reflectance and transmittance calculated by CTMC and DISORT are up to $\xi_R = 0.10$ (*ws*) and $\xi_{Tr} = 0.29$ (*mI*), respectively, independent of the radiative boundary condition (collimated or diffuse incident radiative flux). DISORT's lower *R* values are mainly due to simplifications in the radiative transfer model while DISORT's larger *Tr* values are due to simplifications in both the snow morphology and the radiative transfer model.

[34] Our results provide evidence that simplified morphology and simplified radiative transfer model introduce significant errors in the calculation of the effective radiative properties of snow at visible and NIR wavelengths, especially for snow with low porosity. The interaction of radiation with snow is inherently complicated because of the complex and varying snow morphology. More detailed and precise measurements could be useful to validate the predictions by CT-based multiphase models.

[35] In summary, CTMC.

[36] 1. Offers a novel multiscale methodology for determining the macroscopic optical properties of snow based on its complex microstructure and a multiphase radiative heat transfer model.

[37] 2. Allows quantifying the changes in macroscopic radiative properties resulting from changes or simplifications in morphology, and simplifications in the heat transfer model (homogenized versus multiphase).

[38] 3. Enables in-depth analysis of radiative heat transfer at the pore-level scale, which is not possible by the commonly applied DISORT model or any spatially averaged continuum model. Consequently, the investigation of completely new sets of research problems are possible, where detailed radiative characterization at the pore-level scale is crucial, e.g., snow cover instabilities due to inhomogeneous irradiation.

[39] 4. Permits straightforward characterization of the optical properties of snow containing impurities (e.g., bubbles inside the ice grain, soot and dust inside or in between the ice grains) based on physical, nonnegative [*Mullen and Warren*, 1988] intrinsic radiation properties of the impurities and realistic impurities distribution within the particle (multiple particles or agglomerates) [*Jacobson*, 2004].

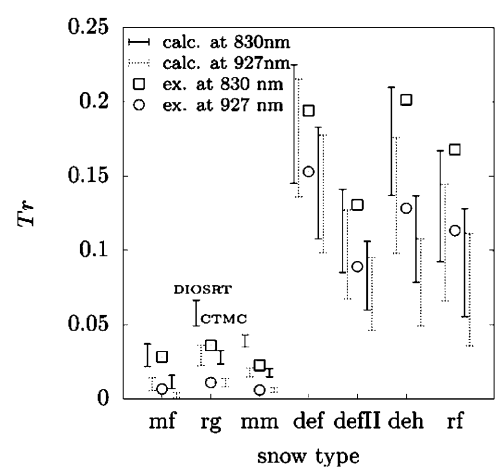


**Figure 14.** Experimentally measured transmittance at $\lambda = 0.830$ and 0.927 $\mu$m and the numerically calculated values by DISORT (left of experimental data points) and CTMC (right of experimental data points) for seven types of snow samples (Table 4).

**Table A1.** Relative Difference, $\Delta$, of $R$ and $Tr$ for the Five Characteristic Snow Types Calculated by the CTMC Model, by Monte Carlo for IOSS With Equal $A_0$ and $\varepsilon$, and by the DISORT Model for $\lambda$ = 0.5, 0.8, 1, 1.3, and 1.5 $\mu$m

| $\lambda$ ($\mu$m) | Snow Type | CTMC versus $A_0/\varepsilon$-IOSS | | CTMC versus DISORT | | DISORT versus $A_0/\varepsilon$-IOSS | |
|---|---|---|---|---|---|---|---|
| | | $\Delta_R$ | $\Delta_{Tr}$ | $\Delta_R$ | $\Delta_{Tr}$ | $\Delta_R$ | $\Delta_{Tr}$ |
| 0.5 | Ds | 0.0044 | 0.0678 | 0.0238 | 0.3618 | 0.0199 | 0.2158 |
| | mI | 0.0160 | 0.2312 | 0.0424 | 0.6088 | 0.0275 | 0.2347 |
| | mII | 0.0095 | 0.1038 | 0.0420 | 0.4535 | 0.0339 | 0.2406 |
| | Dh | 0.0102 | 0.0520 | 0.0746 | 0.3834 | 0.0916 | 0.3147 |
| | ws | 0.0154 | 0.0857 | 0.0688 | 0.3836 | 0.0904 | 0.3392 |
| | Ds | 0.0005 | 0.1169 | 0.0256 | 0.3394 | 0.0257 | 0.1661 |
| | mI | 0.0095 | 0.3292 | 0.0423 | 0.6566 | 0.0343 | 0.1976 |
| 0.8 | mII | 0.0061 | 0.1464 | 0.0464 | 0.4518 | 0.0423 | 0.2104 |
| | Dh | 0.0114 | 0.0488 | 0.0818 | 0.4079 | 0.1014 | 0.3244 |
| | ws | 0.0184 | 0.1022 | 0.0860 | 0.4432 | 0.1143 | 0.3779 |
| | Ds | 0.0139 | 0.4493 | 0.0603 | 0.3730 | 0.0790 | 0.0556 |
| | mI | 0.0116 | 1.1602 | 0.0784 | 1.2109 | 0.0976 | 0.0229 |
| 1 | mII | 0.0061 | 0.4362 | 0.0994 | 0.5513 | 0.1172 | 0.0742 |
| | Dh | 0.0238 | 0.0566 | 0.1530 | 0.5613 | 0.2087 | 0.3958 |
| | ws | 0.0406 | 0.1727 | 0.2022 | 0.7781 | 0.3043 | 0.5347 |
| | Ds | 0.0362 | 1.6824 | 0.1329 | 0.2294 | 0.1951 | 1.1818 |
| | mI | 0.0347 | 6.0175 | 0.1712 | 3.0009 | 0.2485 | 0.7540 |
| 1.3 | mII | 0.0178 | 1.5690 | 0.2173 | 0.7409 | 0.3004 | 0.4756 |
| | Dh | 0.0599 | 0.1196 | 0.3070 | 1.0468 | 0.5294 | 0.5699 |
| | ws | 0.1018 | 0.1429 | 0.3809 | 3.2764 | 0.7796 | 0.7996 |
| | Ds | 0.1685 | - | 0.4578 | - | 1.1549 | - |
| | mI | 0.1604 | - | 0.5154 | - | 1.3943 | - |
| 1.5 | mII | 0.0812 | - | 0.5620 | - | 1.4685 | - |
| | Dh | 0.0757 | - | 0.5322 | - | 1.2994 | - |
| | ws | 0.0380 | - | 0.4262 | - | 0.6766 | - |

[40] 5. Allows for the characterization of snow composed of stratified slabs of different snow types.

[41] 6. Enables studies on variations in the angular and spatial distribution of the incident radiation, e.g., accounting for atmospheric interaction processes or inclined irradiation.

## Appendix A

[42] The relative difference between $R$ and $Tr$,

$$\Delta_{R,\lambda} = \frac{\left|R_{\mathrm{IOSS,type}_i} - R_{\mathrm{CT/DISORT}}\right|}{R_{\mathrm{CT/DISORT}}}, \tag{A1}$$

$$\Delta_{Tr,\lambda} = \frac{\left|Tr_{\mathrm{IOSS,type}_i} - Tr_{\mathrm{CT/DISORT}}\right|}{Tr_{\mathrm{CT/DISORT}}}, \tag{A2}$$

calculated by the CTMC model, by Monte Carlo on 3 types of IOSS, and by the DISORT model for $\lambda$ = are depicted in Table A1.

## Notation

$A$ overall absorptance
$A_0$ specific surface, m$^{-1}$
$d$ particle diameter, m
$f$ size distribution function, m$^{-1}$
$g$ asymmetry factor
$I$ averaged radiative intensity, W m$^{-2}$ sr$^{-1}$ $\mu$m$^{-1}$
$k$ imaginary part of complex refractive index
$l$ length, m
$L$ pore-scale radiative intensity, W m$^{-3}$ sr$^{-1}$
$m$ complex refractive index
$n$ real part of complex refractive index
$n_V$ number density, m$^{-3}$
$q$ heat flux, W m$^{-2}$
$r$ relative difference
$R$ overall reflectance
$\hat{\mathbf{s}}$ unit vector of path direction
$T$ temperature, K
$Tr$ overall transmittance
$V$ total sample volume, m$^3$
$\mathbf{x}$ position vector for spatial coordinates in the sample, m

Greek

$\beta$ extinction coefficient, m$^{-1}$
$\delta$ Dirac delta function
$\Delta$ relative difference
$\varepsilon$ porosity
$\varepsilon_r$ emissivity
$\kappa$ absorption coefficient, m$^{-1}$
$\lambda$ radiation wavelength, m
$\mu_s$ cosine of scattering angle
$\xi$ normalized 2-norm
$\rho''$ bi-directional reflectivity
$\sigma_s$ scattering coefficient, m$^{-1}$
$\Phi$ scattering phase function
$\omega$ scattering albedo
$\Omega$ solid angle, sr

Subscripts

a absorption
att attenuated
m mean
b blackbody
d difference of the azimuthal angles
dif difference
ex experimental
$i, j$ phase indices (1 = void, 2 = solid)
in incoming
int internal
op opening
refl reflection
refr refraction
s scattering
tot total
vox voxel
$\lambda$ spectral
$\infty$ initial

Abbreviations

ASD analytical spectral device
CT computed tomography
CTMC CT-based MC model
ds decomposed snow
def decomposed and fragmented
deh depth hoar
dh depth hoar
DISORT discrete ordinate method on OED spheres
DPLS direct pore-level simulation
ICSSG International classification for seasonal snow on the ground
IOSS identical overlapping semitransparent spheres
mI metamorphosed I

mII metamorphosed II
mf melt forms
mm machined made
MC Monte Carlo
ns natural snow
NIR near infrared
OED optical equivalent grain size
rg rounded grains
rm round melted
REV representative elementary volume
RTE radiative transfer equation
VNIR visible near infrared
ws wet snow

[43] **Acknowledgments.** This work has been financially supported by the Swiss National Science Foundation under contract 200021–115888 and by the European Commission under contract 212470 (Project HYCYCLES).

## References

Aoki, T., T. Aoki, M. Fukabori, A. Hachikubo, Y. Tachibana, and F. Nishio (2000), Effects of snow physical parameters on spectral albedo and bidirectional reflectance of snow surface, *J. Geophys. Res.*, *105*, 10,219–10,236, doi:10.1029/1999JD901122.

Bänniger, D., C. Bourgeois, M. Matzl, and M. Schneebeli (2008), Reflectance modeling for real snow structures using a beam tracing model, *Sensors*, *8*, 3482–3496, doi:10.3390/s8053482.

Beaglehole, D., B. Ramanathan, and J. Rumberg (1998), The UV to IR transmittance of Arctic snow, *J. Geophys. Res.*, *103*, 8849–8857, doi:10.1029/97JD03604.

Berryman, J., and S. Blair (1986), Use of digital image analysis to estimate fluid permeability of porous material: Application of two-point correlation functions, *J. Appl. Phys.*, *60*, 1930–1938, doi:10.1063/1.337245.

Bohren, C., and D. Huffman (2004), *Absorption and Scattering of Light by Small Particles*, 3rd ed., John Wiley, New York.

Born, M., and E. Wolf (1999), *Principles of Optics*, 7th ed., Cambridge Univ. Press, New York.

Dominé, F., T. Lauzier, A. Cabanes, L. Legagneux, W. Kuhs, K. Techmer, and T. Heinrichs (2003), Snow metamorphism as revealed by scannin electron microscopy, *Microsc. Res. Tech.*, *62*, 33–48, doi:10.1002/jemt.10384.

Douville, H., J.-F. Royer, and J.-F. Mahfouf (1995), A new snow parametrization for the Météo-France climate model, Part 1: validation in stand-alone experiments, *Clim. Dyn.*, *12*, 21–35, doi:10.1007/BF00208760.

Farmer, J. T., and J. R. Howell (1998), Comparison of Monte Carlo strategies for radiative transfer in participating media, *Adv. Heat Transfer*, *31*, 333–429, doi:10.1016/S0065-2717(08)70243-0.

Fierz, C., R. Armstrong, Y. Durand, P. Etchevers, E. Greene, D. McClung, K. Nishimura, P. Satyawali, and S. Sokratov (2009), *The International Classification of Seasonal Snow on the Ground*, *Tech. Doc. in Hydrol.*, vol.83, UNESCO-IHP, Paris.

Fily, M., B. Bourdelles, J. Dedieu, and C. Sergent (1997), Comparison of in situ and Landsat Thematic Mapper derived snow grain characteristics in the Alps, *Remote Sens. Environ.*, *59*, 452–460.

Flanner, M. G., and C. S. Zender (2006), Linking snowpack microphysics and albedo evolution, *J. Geophys. Res.*, *111*, D12208, doi:10.1029/2005JD006834.

Flin, F., J.-B. Brzoska, B. Lesaffre, C. Coléou, and A. Pieritz (2004), Three-dimensional geometric measurements of snow microstructural evolution under isothermal conditions, *Ann. Glaciol.*, *38*, 39–44, doi:10.3189/172756404781814942.

Foster, J., and A. Rango (1989), Advances in modeling of snowpack processes utilizing remote sensing technology, *GeoJournal*, *19*, 185–192, doi:10.1007/BF00174648.

Gallet, J.-C., F. Domine, C. Zender, and G. Picard (2009), Measurements of the specific surface area of snow using infrared reflectance in an integrating sphere at 1310 and 1550 nm, *Cryosphere*, *3*, 167–182, doi:10.5194/tc-3-167-2009.

Gardner, A., and M. Sharp (2010), A review of snow and ice albedo and the development of a new physically based broadband albedo parameterization, *J. Geophys. Res.*, *115*, F01009, doi:10.1029/2009JF001444.

Gergely, M., M. Schneebeli, and K. Roth (2010), First experiments to determine snow density from diffuse near-infrared transmittance, *Cold Reg. Sci. Technol.*, *64*, 81–86, doi:10.1016/j.coldregions.2010.06.005.

Glendinning, J., and E. Morris (1999), Incorporation of spectral and directional radiative transfer in a snow model, *Hydrol. Processes*, *13*, 1761–1772, doi:10.1002/(SICI)1099-1085(199909)13:12/13<1761::AID-HYP856>3.0.CO;2-Y.

Good, W. (1987), Thin sections, serial cuts and 3D analysis of snow, *IAHS Publ.*, *162*, 35–48.

Grenfell, T., and S. Warren (1999), Representation of a nonspherical ice particle by a collection of independent spheres for scattering and absorption of radiation, *J. Geophys. Res.*, *104*, 31,697–31,709, doi:10.1029/1999JD900496.

Haussener, S., and A. Steinfeld (2012), Effective heat and mass transport properties of anisotropic porous ceria for solar thermochemical fuel generation, *Materials*, *5*, 192–209, doi:10.3390/ma5010192.

Haussener, S., W. Lipiński, J. Petrasch, P. Wyss, and A. Steinfeld (2009), Tomographic characterization of a semitransparent-particle packed bed and determination of its thermal radiative properties, *J. Heat Transfer*, *131*, 072701, doi:10.1115/1.3109261.

Haussener, S., P. Coray, W. Lipiński, P. Wyss, and A. Steinfeld (2010a), Tomography-based heat and mass transfer characterization of reticulate porous ceramics for high-temperature processing, *J. Heat Transfer*, *132*, 023305, doi:10.1115/1.4000226.

Haussener, S., W. Lipiński, P. Wyss, and A. Steinfeld (2010b), Tomography-based analysis of radiative transfer in reacting packed beds undergoing a solid-gas thermochemical transformation, *J. Heat Transfer*, *132*, 061201, doi:10.1115/1.4000749.

Jacobson, M. Z. (2004), The climate response of fossil-fuel and biofuel soot, accounting for soot's feedback to snow and sea ice albedo and emissivity, *J. Geophys. Res.*, *109*, D21201, doi:10.1029/2004JD004945.

Jin, Z., and J. Simpson (1999), Bidirectional anisotropic reflectance of snow and sea ice in AVHRR channel 1 and 2 spectral regions-Part I: Theoretical analysis, *IEEE Trans. Geosci. Remote Sens.*, *37*, 543–555.

Kaempfer, T. U., M. A. Hopkins, and D. K. Perovich (2007), A three-dimensional microstructure-based photon-tracking model of radiative transfer in snow, *J. Geophys. Res.*, *112*, D24113, doi:10.1029/2006JD008239.

Kerbrat, M., B. Pinzer, T. Huthwelker, H. Gäggeler, M. Ammann, and M. Schneebel (2008), Measuring the specific surface area of snow with X-ray tomography and gas adsorption: comparison and implifications for surface smoothness, *Atmos. Chem. Phys.*, *8*, 1261–1275, doi:10.5194/acp-8-1261-2008

Kuipers Munneke, M., M. van der Broeke, C. Reijmer, M. Helsen, and M. Schneebeli (2009), The role of radiation penetration in the energy budget of the snowpack at Summit, Greenland, *Cryosphere*, *3*, 155–165, doi:10.5194/tc-3-155-2009.

Lipiński, W., J. Petrasch, and S. Haussener (2010a), Application of the spatial averaging theorem to radiative heat transfer in two-phase media, *J. Quant. Spectrosc. Radiat. Transf.*, *111*, 253–258, doi:10.1016/j.jqsrt.2009.08.001.

Lipiński, W., D. Keene, S. Haussener, and J. Petrasch (2010b), Continuum radiative transfer modeling in media consisting of optically distinct components in the limit of geometrical optics, *J. Quant. Spectrosc. Radiat. Transf.*, *111*, 2474–2480, doi:10.1016/j.jqsrt.2010.06.022.

Marks, D., and J. Dozier (1992), Climate and energy exchange at the snow surface in the Alpine Region of the Sierra Nevada: 2. Snow cover energy balance, *Water Resour. Res.*, *28*, 3043–3054, doi:10.1029/92WR01483.

Marks, D., J. Kimball, D. Tingey, and T. Link (1998), The sensitivity of snowmelt processes to climate conditions and forest cover during rain-on-snow: A case study of the 1996 Pacific Northwest flood, *Hydrol. Processes*, *12*, 1569–1587, doi:10.1002/(SICI)1099-1085(199808/09)12:10/11<1569::AID-HYP682>3.0.CO;2-L.

Matzl, M., and M. Schneebeli (2006), Measuring specific surface area of snow by near-infrared photography, *J. Glaciol.*, *52*, 558–564, doi:10.3189/172756506781828412.

Mishchenko, M. I. (1994), Asymmetry parameters of the phase function for densely packed scattering Grains, *J. Quant. Spectrosc. Radiat. Transf.*, *52*, 95–110, doi:10.1016/0022-4073(94)90142-2.

Mishchenko, M. I. (2008), Multiple scattering, radiative transfer, and weak localization in discrete random media: unified microphysical approach, *Rev. Geophys.*, *46*, RG2003, doi:10.1029/2007RG000230.

Mishchenko, M. I., and A. Macke (1997), Asymmetry parameters of the phase function for isolated and densely packed spherical particles with multiple internal inclusions in the geometric optics limit, *J. Quant. Spectrosc. Radiat. Transf.*, *57*, 767–794, doi:10.1016/S0022-4073(97)00012-5.

Mishchenko, M. I., V. P. Tishkovets, L. D. Travis, B. Cairns, J. M. Dlugach, L. Liu, V. K. Rosenbush, and N. N. Kiselev (2011), Electromagnetic scattering by a morphologically complex object: fundamental concepts and common misconceptions, *J. Quant. Spectrosc. Radiat. Transf.*, *112*, 671–692, doi:10.1016/j.jqsrt.2010.03.016.

Modest, M. (2003), *Radiative Heat Transfer*, 2nd ed., Academic, San Diego, Calif.

Mullen, P., and S. Warren (1988), Theory of the optical properties of lake ice, *J. Geophys. Res.*, *93*, 8403–8414, doi:10.1029/JD093iD07p08403.

Nolin, A., and J. Dozier (2000), A hyperspectral method for remotely sensing the grain size of snow, *Remote Sens. Environ.*, *74*, 207–216, doi:10.1016/S0034-4257(00)00111-5.

Painter, T., and J. Dozier (2004), Measurements of the hemispherical-direcitonal reflectance of snow at fine spectral and angular resolution, *J. Geophys. Res.*, *109*, D18115, doi:10.1029/2003JD004458.

Painter, T., N. Molotch, M. Cassidy, M. Flanner, and K. Steffen (2007), Contact spectroscopy for determination of stratigraphy of snow optical grain size, *J. Glaciol.*, *53*, 121–127, doi:10.3189/172756507781833947.

Petrasch, J., P. Wyss, and A. Steinfeld (2007), Tomography-based Monte Carlo determination of radiative properties of reticulate porous ceramics, *J. Quant. Spectrosc. Radiat. Transf.*, *105*, 180–197, doi:10.1016/j.jqsrt.2006.11.002.

Petrasch, J., S. Haussener, and W. Lipiński (2011), Discrete vs. continuum level simulations of radiative transfer in semitransparent two-phase media, *J. Quant. Spectrosc. Radiat. Transf.*, *112*, 1450–1459, doi:10.1016/j.jqsrt.2011.01.025.

Picard, G., L. Arnaud, F. Domine, and M. Fily (2009), Determining snow specific surface area from near-infrared reflectance measurements: Numerical study on the influence of grain shape, *Cold Reg. Sci. Technol.*, *56*, 10–17, doi:10.1016/j.coldregions.2008.10.001.

Roesch, A., M. Wild, R. Pinker, and A. Ohmura (2002), Comparison of spectral surface albedos and their impact on the general circulation model simulated surface climate, *J. Geophys. Res.*, *107*(D14), 4221, doi:10.1029/2001JD000809.

Rothman, L. (2005), The HITRAN-2004 molecular spectroscopic database, *J. Quant. Spectrosc. Radiat. Transf.*, *96*, 139–204, doi:10.1016/j.jqsrt.2004.10.008.

Schneebeli, M., and S. Sokratov (2004), Tomography of temperature gradient metamorphism of snow and associated changes in heat conductivity, *Hydrol. Processes*, *18*, 3655–3665, doi:10.1002/hyp.5800.

Stamnes, K., S. Tsay, W. Wiscombe, and K. Jayaweera (1988), Numerical stable algorithm for discrete-ordinate-method radiative transfer in multiple scattering and emitting layered media, *Appl. Opt.*, *27*, 2502–2509, doi:10.1364/AO.27.002502.

Tancrez, M., and J. Taine (2004), Direct identification of absorption and scattering coefficients and phase function of a porous medium by a Monte Carlo technique, *Int. J. Heat Mass Transfer*, *47*, 373–383, doi:10.1016/S0017-9310(03)00146-7.

Warren, S., and E. Brandt (2008), Optical constants of ice from the ultraviolet to the microwave: A revised compilation, *J. Geophys. Res.*, *113*, D14220, doi:10.1029/2007JD009744.

Warren, S., R. Brandt, and T. Grenfell (2006), Visible and near-ultraviolet absorption spectrum of ice from transmission of solar radiation into snow, *Appl. Opt.*, *45*, 5320–5334, doi:10.1364/AO.45.005320.

Wiscombe, W., and S. Warren (1980), A model for the spectral albedo of snow. I. Pure snow, *J. Atmos. Sci.*, *37*, 2712–2733, doi:10.1175/1520-0469(1980)037<2712:AMFTSA>2.0.CO;2.

Xie, Y., P. Yang, B.-C. Gao, G. Kattawar, and I. Mishchenko (2006), Effect of the ice crystal shape and effectie size on snow bidirectional reflectance, *J. Quant. Spectrosc. Radiat. Transf.*, *100*, 457–469, doi:10.1016/j.jqsrt.2005.11.056.